



Production of high purity H₂ through chemical-looping water–gas shift at reforming temperatures – The importance of non-stoichiometric oxygen carriers

Christopher de Leeuwe^{a,b}, Wenting Hu^a, John Evans^c, Moritz von Stosch^a, Ian S Metcalfe^{a,*}

^a School of Engineering, Newcastle University, Newcastle upon Tyne, NE1 7RU, UK

^b Department of Chemical Engineering and Analytical Science, The University of Manchester, Manchester, M1 3AL, UK

^c Department of Chemistry, Durham University, Durham, DH1 3LE, UK

ARTICLE INFO

Keywords:

Hydrogen production
Reactor modelling
Chemical looping
Carbon capture and storage

ABSTRACT

H₂ is an important feedstock for many industrial processes and could be used as an energy carrier in a low carbon economy. This means that carbon neutral methods for H₂ production are of vital importance. Chemical looping allows for H₂ production with inherent carbon separation, making it an ideal system to produce low carbon H₂. This work generates insights into the production of high purity H₂ using a chemical looping packed bed reactor system containing an oxygen carrier of variable oxygen non-stoichiometry. Such a system has been shown to achieve 95% conversion of H₂O to H₂ at 1073 K outperforming the maximum theoretical conversions of 50% achieved by a conventional water gas shift reactor at that temperature. A numerical model was developed from theoretical consideration, with no fitted parameters and used to simulate the working reactor.

Operando measurement of gas conversions and changes in solid oxygen capacity, through synchrotron X-ray diffraction, were used to validate the numerical model and confirmed that the reaction was thermodynamically limited. The model the model was shown to reproduce the conversion of the oxygen carrier, the reactant conversion and the product evolution.

Sensitivity analysis showed that the relationship between the oxygen carrier material oxygen content and the chemical potential of oxygen in the carrier was the key consideration for the design and operation of a packed bed chemical looping reactor using an oxygen carrier of variable non-stoichiometry.

Nomenclature

Symbol	Description	Units
A	Empirical constant	\AA K^{-2}
B	Empirical constant	\AA K^{-1}
C	Empirical constant	\AA
D_{axCO}	The axial diffusivity of CO in Ar for the packed bed	$\text{m}^2 \text{s}^{-1}$
D_{axCO_2}	The axial diffusivity of CO ₂ in Ar for the packed bed	$\text{m}^2 \text{s}^{-1}$
D_{axH_2}	The axial diffusivity of H ₂ in Ar for the packed bed	$\text{m}^2 \text{s}^{-1}$
D_{axH_2O}	The axial diffusivity of H ₂ O in Ar for the packed bed	$\text{m}^2 \text{s}^{-1}$
$D_{Ar,i}$	The axial diffusivity of <i>i</i> in Ar	$\text{m}^2 \text{s}^{-1}$
K_c	Equilibrium constant for oxidation of CO to CO ₂ by $\frac{1}{2}\text{O}_2$	–
K_{Fe}	Equilibrium constant for Eq. (17)	–
K_H	Equilibrium constant for reduction of H ₂ O to H ₂ producing $\frac{1}{2}\text{O}_2$	–
K_{ox}	Equilibrium constant for Eq. (18)	–
L	Length of the reactor	m

(continued on next column)

(continued)

Symbol	Description	Units
Pe	Peclet number	–
P_{O_2}	Partial pressure of O ₂	bar
T	Temperature	K
U	Superficial velocity	m s^{-1}
<i>a</i>	Unit cell parameter	\AA
d_{tube}	Reactor diameter	m
r_{CO}	Rate of consumption of CO	$\text{mol m}^{-3} \text{s}^{-1}$
r_{H_2O}	Rate of consumption of H ₂ O	$\text{mol m}^{-3} \text{s}^{-1}$
t	Time	s
u	Molar flux during the reduction half cycle	$\text{mol m}^{-2} \text{s}^{-1}$
v	Molar flux during the oxidation half cycle	$\text{mol m}^{-2} \text{s}^{-1}$

(continued on next page)

* Corresponding author.

E-mail address: ian.metcalfe@newcastle.ac.uk (I.S. Metcalfe).

<https://doi.org/10.1016/j.cej.2021.130174>

Received 15 February 2021; Received in revised form 26 April 2021; Accepted 29 April 2021

Available online 7 May 2021

1385-8947/© 2021 The Author(s). Published by Elsevier B.V. This is an open access article under the CC BY license (<http://creativecommons.org/licenses/by/4.0/>).

(continued)

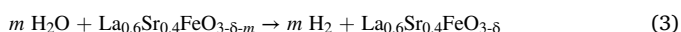
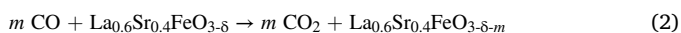
Symbol	Description	Units
x	Extent of substitution of La by Sr	mol mol ⁻¹
y_i	Mole fraction of species i	mol mol ⁻¹
y_c	Total mole fraction of carbon containing gases	mol mol ⁻¹
y_H	Total mole fraction of hydrogen containing gases	mol mol ⁻¹
z	Distance down the reactor	m
δ	Oxygen non-stoichiometry of perovskite	mol mol ⁻¹
ϵ	Voidage of the bed	-
ν_i	Diffusion volume of species i	-
$\hat{\rho}_g$	Molar density of the gas phase	mol m ⁻³
$\hat{\rho}_s$	Molar density of the solid phase	mol m ⁻³

1. Introduction

H₂ is an important feed stock for many industrial processes as well as a potential energy carrier for transportation [1]. Approximately 60 million tonnes of H₂ is produced annually, the majority of which is derived from fossil fuel using processes such as steam methane reforming, cracking of hydrocarbons and gasification of coal followed by water gas shift reactions [2]. The product stream from these processes normally consists of a mixture of H₂ and carbon-containing species, mostly CO₂, and requires further separation before use [3,4].

Conventional water gas shift reactors are a mature, efficient and well developed technology and can achieve high conversion of H₂ but require low temperatures (~473 K) where the thermodynamics allow for higher conversion, but the kinetics are less favourable. This requires large catalytic reactors, highly optimised catalysts and, for H₂ production from methane reforming, requires the gas stream to be cooled from around 1073 K. Additionally, if pure H₂ via carbon capture, is required then expensive and energy-intensive separation processes such as pressure swing adsorption are needed.

In comparison chemical looping systems allow for H₂ production with inherent separation of the product gases by splitting the relevant homogeneous redox reaction into two or more heterogeneous reactions through the use of a solid oxygen carrier material (OCM) [5–9]. For example, the water–gas shift reaction Eq. (1), which is exploited in the conventional H₂ production process, can be implemented in chemical looping mode as follows. The OCM (here exemplified by the perovskite modelled in this work, La_{0.6}Sr_{0.4}FeO_{3- δ}) first reacts with CO Eq. (2) and is subsequently re-oxidised by H₂O to produce H₂ Eq. (3), so that the carbon-containing gases are never in contact with the H₂O and/or H₂ and the need for separation is eliminated.



The inherent separation of the gas reactants can be carried out spatially by moving the OCM between different fluidised bed reactors, which are continuously fed with the appropriate gas, allowing for continuous production of the products [10,11]. Fan details the complexities in the design and operation of such a system, which requires solid transport and gas locks to avoid contamination in the reactors [12].

Alternatively, the reactions can be separated temporally, with a packed bed being fed alternately with the reducing and oxidising gases [13,14]. To continuously produce H₂ using this method, at least two packed bed reactors must be employed. The design of packed bed systems requires less solid processing equipment but high temperature switching valves are required for the gas streams. Previous work has shown that chemical looping H₂ production in such systems using oxides with variable non-stoichiometry can produce high purity H₂ and CO₂ (H₂:H₂O and CO:CO₂ > 19:1 at the reactor outlets, on a molar basis) at temperatures around 1100 K [15]. This is in contrast to the homogeneous water–gas shift reaction scheme which is limited by the gas-phase equilibrium (the

equilibrium constant for Eq. (1) at 1100 K is close to unity [16]) or indeed a chemical looping process exploiting a single phase transition in a metal–metal oxide system. To achieve this, the system must operate in a counter-current packed bed. A schematic showing the different steps the reactor passes through is shown in Fig. 1. The oxidising and reducing gases must flow in opposite directions inside the reactor, so that the conversion to the products can be maximised. More importantly, the process in ref. [15] exploits non-stoichiometric oxides, the oxygen content of which varies continuously with the oxygen chemical potential. The non-stoichiometric OCM, La_{0.6}Sr_{0.4}FeO_{3- δ} , was chosen for its stability over a wide range of partial pressures of oxygen, P_{O_2} , and the fact that the dependence of the oxygen non-stoichiometry, δ , on P_{O_2} for this material is well documented [17–19]. Additionally the relationship between unit cell parameter and oxygen content has been studied in detail [20]. This means that when *operando* synchrotron powder X-ray diffraction is performed on a working reactor, the oxygen content of the carrier as a function of time can be determined.

The dependence of oxygen content of such non-stoichiometric oxides on the oxygen chemical potential, while useful in practice, significantly complicates the numerical modelling of such a reactor. Packed bed systems using conventional oxygen carriers which undergo set phase changes (e.g. nickel or iron and their oxides) are commonly modelled with a reaction wave propagating through the bed along with the phase change [21–23]. In this system, however, there are no phase transitions at fixed oxygen chemical potentials accompanying the gas–solid reaction. Thus, a different approach is needed to represent the reactor.

In this work, a numerical model for chemical-looping H₂ production using the non-stoichiometric oxide La_{0.6}Sr_{0.4}FeO_{3- δ} in a packed bed reactor was developed from first principles and model results were validated against the corresponding experiments. Sensitivity analysis was carried out to assess the influence of key design parameters on a working reactor such as operating conditions, inlet conditions and the relationship between the OCM's oxygen content and equivalent oxygen partial pressure on the purity of products obtained and overall conversion of reactants. This information will be of crucial importance in the scale up of reactor design.

2. Materials and methods

2.1. Material synthesis

La_{0.6}Sr_{0.4}FeO_{3- δ} was synthesised using the Pechini method [24] detailed by de Leeuwe *et al* [20].

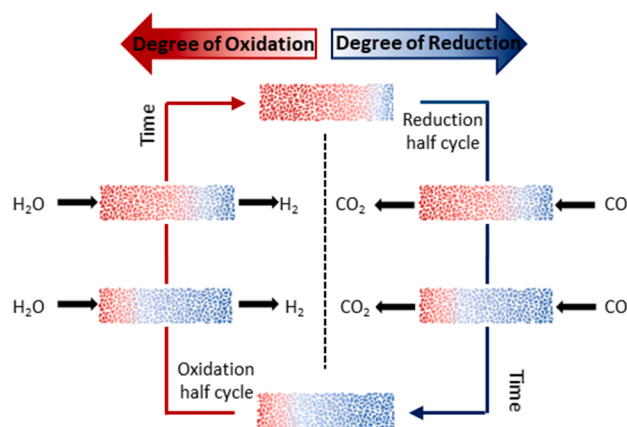


Fig. 1. A schematic of how a single chemical looping reactor bed using a non-stoichiometric oxide produces high purity H₂.

2.2. Flow system

The experimental set up used to test the validity of the numerical model was detailed by Metcalfe et al. [15]

Studies were carried out using a horizontal reactor with an internal diameter (d_{tube}) of 7 mm, the first of which involved the cycling of $\text{La}_{0.6}\text{Sr}_{0.4}\text{FeO}_{3-\delta}$ 1100 times at 1093 K with alternating feeds of pre-heated 5% CO and 5% H_2O , both in a balance of Ar, each having a flowrate of 50 ml min^{-1} (measured at standard temperature and pressure, STP) lasting for 1 min, in order to determine the long-term stability of the material. Experiments consisting of 30 redox cycles were also performed at temperatures between 993 K and 1193 K in the same reactor to determine the response of the system to temperature.

To further validate the model, a system of redox buffer gases, ($2.5 \pm 0.125 \text{ mol\% CO}_2$ with $2.5 \pm 0.125 \text{ mol\% CO}$ and $0.5 \pm 0.025 \text{ mol\% CO}_2$ with $5 \pm 0.25 \text{ mol\% CO}$ in a balance of Ar) was used to reduce and oxidise a working reactor bed, such that the thermodynamics of the system were well defined at every point in the reactor. This was performed in a vertical packed bed with a d_{tube} of 4 mm in conjunction with *operando* synchrotron X-ray diffraction, described in detail in the next section.

Regardless of reactors and operating conditions used, one complete redox cycle contained six segments: feed the reducing gas of 5% CO, or 5% CO and 0.5% CO_2 , in the “forward” direction; purge the reactor with Ar, also in the “forward” direction; switch the Ar flow to “backward” direction; feed the oxidising gas of 5% H_2O , or 2.5% CO and 2.5% CO_2 , in the “backward” direction; purge with Ar in the “backward” direction and finally purge with Ar in the “forward” direction. The compositions of the reactive gases have an uncertainties less than 5% of the quoted values in each case. The outlet gas compositions were analysed using a quadrupole mass spectrometer (Hiden, QGA). The complete methodology used for gas phase calculations was detailed in the SI of de Leeuwe et al. [20]

2.3. Operando XRD

Operando synchrotron powder X-ray diffraction (SXRD) was conducted on a working reactor bed using beamline ID22 at the European Synchrotron Research Facility (ESRF, experiment numbers MA2914, MA3410 and MA4239) in transmission geometry with an X-ray energy of $\sim 35 \text{ keV}$ and a spot size of approximately $1 \text{ mm} \times 1 \text{ mm}$. A nine crystal multi-analyser stage [25] was used for fast data acquisition in the 2θ range of 1 to 19.2° . The scan time varied between 7 and 31 s, corresponding to scan rates between 30 and 12 degrees per minute. SXRD data were collected from 16 locations uniformly distributed along the bed, 11.3 mm apart.

The system was operated in a vertical orientation with a furnace set point of 1093 K for *operando* X-ray diffraction studies. 2.2 g of $\text{La}_{0.6}\text{Sr}_{0.4}\text{FeO}_{3-\delta}$ in the size fraction 80–160 μm and 0.4 g Y_2O_3 powder sieved to less than 40 μm was packed into a quartz reactor with an d_{tube} of 4 mm, resulting in a bed height of 170 mm. The gases were all regulated at 50 ml min^{-1} STP and the system was operated at 2 bar absolute.

The inert nature of Y_2O_3 in the range of P_{O_2} studied here [26], together with its Bragg peaks not coinciding with major peaks from $\text{La}_{0.6}\text{Sr}_{0.4}\text{FeO}_{3-\delta}$, makes it useful as an internal standard to infer the temperature of the reactor. The temperature was obtained using empirical equations linking unit cell parameter to temperature [26,27].

The temperature measurement from the fitting of the Y_2O_3 peaks was based on cell parameter data published in Refs. [26,27] using the expression:

$$T = \frac{(-B + (B^2 - 4 \times A(C - a_{\text{Y}_2\text{O}_3}))^{0.5})}{2A} \quad (4)$$

$$A = 1.29340 \times 10^{-8} \text{ \AA K}^{-2}$$

$$B = 6.46011 \times 10^{-5} \text{ \AA K}^{-1}$$

$$C = 10.58733218 \text{ \AA}$$

where A , B and C are empirical constants, T is the temperature in kelvin of the sample and $a_{\text{Y}_2\text{O}_3}$ is the unit cell parameter of Y_2O_3 .

Previous work using $\text{La}_{0.6}\text{Sr}_{0.4}\text{FeO}_{3-\delta}$ [20] has linked the unit cell parameter of the material to its temperature and oxygen content. By applying this methodology, it is possible for the oxygen non-stoichiometry, δ , of the material to be linked to the unit cell parameter in this P_{O_2} range and therefore compared to the results of the reactor model.

2.4. Rietveld strategy

Rietveld fitting of the diffraction results was performed using TOPAS v6 (Bruker AXS, Germany)[28,29] using the space group $Pm\bar{3}m$. The unit cell parameter, isotropic temperature factors and a sample strain contribution to the peak shape were refined. The atomic occupancies of La, Sr and Fe were kept constant at 0.6, 0.4 and 1.0, respectively.

3. Model development

The packed bed reactors for H_2 production were modelled under isothermal and isobaric conditions with no fitted parameters. The pressure drop across the bed was sufficiently small (0.01 bar) that it can be neglected, while the assumption of isothermal conditions was examined in more details in this work. It was further assumed that the gas–solid reactions Eqs. (2 and 3) are limited by thermodynamics rather than chemical kinetics or mass transfer processes. Gas flow through the reactor was modelled as plug flow with or without axial dispersion. Side reactions that could lead to carbon deposition were neglected since preliminary investigations showed no carbon deposition in the system (CO or CO_2 in the gas stream during the H_2 production half cycle was below the detection limit of a mole fraction of 10^{-4}). The geometry of the reactor and the reactant flowrates used in the numerical model were based on the corresponding experimental set up described in the experimental section. The thermodynamic data relevant to the system were taken from Kuhn et al. [17]. A full description of the models employed can be found in the SI Sections 1 and 2.

3.1. Modelling the reactor system behaviour

The governing equations for the reduction and oxidation of the solid, i.e. Eqs. (2 and 3), in the packed bed can be written as:

$$-r_{\text{CO}} = u \frac{\partial y_{\text{CO}}}{\partial z} + \varepsilon \hat{\rho}_g \frac{\partial y_{\text{CO}}}{\partial t} - \varepsilon \hat{\rho}_g D_{\text{axCO}} \frac{\partial^2 y_{\text{CO}}}{\partial z^2} \quad (5)$$

$$-r_{\text{H}_2\text{O}} = v \frac{\partial y_{\text{H}_2\text{O}}}{\partial z} + \varepsilon \hat{\rho}_g \frac{\partial y_{\text{H}_2\text{O}}}{\partial t} - \varepsilon \hat{\rho}_g D_{\text{axH}_2\text{O}} \frac{\partial^2 y_{\text{H}_2\text{O}}}{\partial z^2} \quad (6)$$

$$r_{\text{CO}_2} = u \frac{\partial y_{\text{CO}_2}}{\partial z} + \varepsilon \hat{\rho}_g \frac{\partial y_{\text{CO}_2}}{\partial t} - \varepsilon \hat{\rho}_g D_{\text{axCO}_2} \frac{\partial^2 y_{\text{CO}_2}}{\partial z^2} \quad (7)$$

$$r_{\text{H}_2} = v \frac{\partial y_{\text{H}_2}}{\partial z} + \varepsilon \hat{\rho}_g \frac{\partial y_{\text{H}_2}}{\partial t} - \varepsilon \hat{\rho}_g D_{\text{axH}_2} \frac{\partial^2 y_{\text{H}_2}}{\partial z^2} \quad (8)$$

r_{CO} , r_{CO_2} , r_{H_2} and $r_{\text{H}_2\text{O}}$ are the reaction rates of CO, CO_2 , H_2 and H_2O respectively ($\text{mol m}^{-3} \text{ s}^{-1}$); u and v are the molar fluxes of the gas streams ($\text{mol m}^{-2} \text{ s}^{-1}$); y_{CO} , y_{H_2} , y_{CO_2} and $y_{\text{H}_2\text{O}}$ are the mole fractions of CO, H_2 , CO_2 and H_2O in the gas streams (-); $\hat{\rho}_g$ is the molar density of the gas phase (mol m^{-3}); ε is the voidage of the bed (-); z is the axial position along the packed bed (m) and t is the time (s), $D_{\text{ax}i}$ is the axial dispersion coefficient of species i in Ar in a packed bed, where i is CO, CO_2 , H_2O or H_2 . These were determined using correlations given by Levenspiel [30] Eq. (9).

$$D_{\text{ax}i} = D_{\text{Ar},i} + \frac{U^2 \times d_{\text{tube}}^2}{192D_{\text{Ar},i}} \quad (9)$$

$D_{Ar,i}$ is the diffusion coefficient of species i in Ar, U is the superficial velocity of the gas and d_{tube} is the internal diameter of the reactor. The choice of the correct correlation requires knowledge of the geometry of the reactor and the physical properties of the fluid. The viscosity of the fluid was assumed to be that of Ar at 1093 K and 2 bar absolute pressure [31] and the relevant diffusion coefficients were estimated from the interaction between Ar and the gas of interest, using the relationship developed by Fuller *et al.* [32] shown in Eq. (10).

$$D_{Ar,i} = \frac{1 \times 10^{-8} \times T^{1.75} \times \left(\frac{1}{M_{Ar}} + \frac{1}{M_i}\right)^{0.5}}{P \times (\nu_{Ar}^{1/3} + \nu_i^{1/3})^2} \quad (10)$$

Eq. (14) and $P_{O_2}^*$ is the partial pressure of oxygen (P_{O_2}) that would be in equilibrium with the solid phase at the given temperature and δ .



Combining Eqs. (5, 7, 11 and 13), it is possible to obtain the governing equations during the reduction of the OCM.

$$\frac{\partial y_{CO_2}}{\partial t} = \frac{u \frac{\partial y_{CO_2}}{\partial z} - \varepsilon \hat{\rho}_g D_{axCO_2} \frac{\partial^2 y_{CO_2}}{\partial z^2} + (1-\varepsilon) \hat{\rho}_s \frac{d\delta}{dP_{O_2}} \frac{2}{K_C^2} \frac{y_{CO_2}^2}{y_{CO}^3} - \frac{u \frac{\partial y_{CO}}{\partial z} - \varepsilon \hat{\rho}_g D_{axCO} \frac{\partial^2 y_{CO}}{\partial z^2}}{(1-\varepsilon) \hat{\rho}_s \frac{d\delta}{dP_{O_2}} \left(\frac{2}{K_C^2} \frac{y_{CO_2}^2}{y_{CO}^3}\right)} - \varepsilon \hat{\rho}_g}{(1-\varepsilon) \hat{\rho}_s \frac{d\delta}{dP_{O_2}} \left(\frac{2}{K_C^2} \frac{y_{CO_2}^2}{y_{CO}^3}\right) - \varepsilon \hat{\rho}_g} \quad (15)$$

$$\frac{\partial y_{CO}}{\partial t} = \frac{u \frac{\partial y_{CO}}{\partial z} - \varepsilon \hat{\rho}_g D_{axCO} \frac{\partial^2 y_{CO}}{\partial z^2} + (1-\varepsilon) \hat{\rho}_s \frac{d\delta}{dP_{O_2}} \frac{2}{K_C^2} \frac{y_{CO_2}^2}{y_{CO}^3} - \frac{u \frac{\partial y_{CO_2}}{\partial z} - \varepsilon \hat{\rho}_g D_{axCO_2} \frac{\partial^2 y_{CO_2}}{\partial z^2} + (1-\varepsilon) \hat{\rho}_s \frac{d\delta}{dP_{O_2}} \frac{2}{K_C^2} \frac{y_{CO_2}^2}{y_{CO}^3}}{(1-\varepsilon) \hat{\rho}_s \frac{d\delta}{dP_{O_2}} \left(\frac{2}{K_C^2} \frac{y_{CO_2}^2}{y_{CO}^3}\right)} - \varepsilon \hat{\rho}_g}{(1-\varepsilon) \hat{\rho}_s \frac{d\delta}{dP_{O_2}} \left(\frac{2}{K_C^2} \frac{y_{CO_2}^2}{y_{CO}^3}\right) - \varepsilon \hat{\rho}_g} \quad (16)$$

where M is the molar mass of the gas and ν_i is the diffusion volume of the gas.

As the rates of oxygen exchange for similar perovskites are relatively high [33], it was assumed that chemical kinetics are fast and the reaction is thermodynamically limited. This means that the oxygen balance of the solid phase can be linked to the gas phase reaction rates as follows (full details available in sections 1 and 2 of the SI),

$$r_{CO} = -r_{CO_2} = (1-\varepsilon) \hat{\rho}_s \frac{\partial \delta}{\partial t} \quad (11)$$

$$r_{H_2O} = -r_{H_2} = -(1-\varepsilon) \hat{\rho}_s \frac{\partial \delta}{\partial t} \quad (12)$$

where $\hat{\rho}_s$ is the molar density of the solid phase (mol m^{-3}). Furthermore, using the assumption that gas–solid equilibrium is achieved at any location, it can be shown that,

$$\begin{aligned} \frac{\partial \delta}{\partial t} &= \frac{d\delta}{dP_{O_2}^*} \left(\frac{\partial P_{O_2}^*}{\partial y_{CO}} \frac{\partial y_{CO}}{\partial t} + \frac{\partial P_{O_2}^*}{\partial y_{CO_2}} \frac{\partial y_{CO_2}}{\partial t} \right) \\ &= \frac{d\delta}{dP_{O_2}^*} \left(-\frac{2}{K_C^2} \frac{y_{CO_2}^2}{y_{CO}^3} \frac{\partial y_{CO}}{\partial t} + \frac{2}{K_C^2} \frac{y_{CO_2}}{y_{CO}^2} \frac{\partial y_{CO_2}}{\partial t} \right) \end{aligned} \quad (13)$$

where K_C is the equilibrium constant for the oxidation of CO to CO_2

3.2. Modelling the material behaviour

Solving Eqs. (15) and (16) requires the relationship between $P_{O_2}^*$ and the solid phase oxygen content to be defined, in order to determine $\frac{d\delta}{dP_{O_2}^*}$. This can be done through a defect chemistry model describing the following reactions. [17,18]



The model used to define the thermodynamics of the OCM are also described in SI Section 1. Values of K_{Fe} and K_{ox} (equilibrium constants associated with the disproportionation reaction and oxidation of Fe^{3+} ions in the perovskite, respectively) are taken from Mizusaki *et al.* [18] since they agree best with independent experimental measurements [20] in the δ range relevant to this work ($0.19 < \delta < 0.23$).

The defect chemistry model was approximated by a 5th degree polynomial at the given reactor temperature to reduce the computational cost (the equation for the fit at 1093 K is given in Eq. (19) and a comparison of the fit to measured values can be found in SI section 1). This polynomial can then be differentiated to give $\frac{d\delta}{dP_{O_2}^*}$.

$$\begin{aligned} \delta \left(\frac{\log_{10} P_{O_2}^*}{10} \right) &= -3.89761831 \times 10^{-2} \times \left(\frac{\log_{10} P_{O_2}^*}{10} \right)^5 - 0.235225805 \\ &\times \left(\frac{\log_{10} P_{O_2}^*}{10} \right)^4 - 0.591012724 \\ &\times \left(\frac{\log_{10} P_{O_2}^*}{10} \right)^3 - 0.782344918 \\ &\times \left(\frac{\log_{10} P_{O_2}^*}{10} \right)^2 - 0.551282238 \times \left(\frac{\log_{10} P_{O_2}^*}{10} \right) + 3.45065388 \\ &\times 10^{-2} \end{aligned} \quad (19)$$

The approximation was made over a wider range of $0.186 < \delta < 0.3$ for each temperature studied, the value of R^2 for each fit was >0.9999 .

Due to the symmetry of the reduction and oxidation half cycles, the governing equations of the oxidation half cycle resulting from Eqs. (6, 8 and 12) are similar to Eqs. (15 and 16), with u replaced with v , y_{CO} with y_{H_2} , y_{CO_2} with y_{H_2O} , and K_c replaced with $1/K_H$, where K_H is the equilibrium constant for the dissociation of H_2O ,



and with the diffusivities of gases also changed accordingly.

3.3. Simulation conditions and numerical solution

The initial condition of each half cycle was defined so that the P_{O_2} for the gas remaining from the purge in the reactor at the start of each half cycle was the same as that at the end of the preceding half cycle (such that the gas is in equilibrium with the solid at the beginning of each half cycle. Confirmation of this assumption can be found in SI Section 3). For the first half cycle the OCM was assumed to be in equilibrium with $P_{O_2} = 9.38 \times 10^{-8}$ bar (this P_{O_2} is equivalent to that of H_2O at 1093 K, assuming the dissociation of H_2O is at equilibrium). The boundary conditions used were those recommended by Patankar [34]. This states that for a suitably high Peclet number Eq. (21), local one-way behaviour exists at the outflow boundary meaning that diffusion back into the reactor does not occur at the outlet.

$$Pe = \frac{d_{tubc} U}{D_{ax}} \quad (21)$$

For each half cycle the governing equation was transformed into a system of ordinary differential equations using the method of lines by discretisation along the length of the reactor with a backwards difference scheme. The resulting system of ordinary differential equations was solved with ode45 in MATLAB. [35]

The oxidation and the reduction half-cycles were solved sequentially until the system reached steady cyclic operation, where the maximum difference in P_{O_2} at any location in the packed bed in successive cycles during the inert purge was less than 0.001%. This was typically achieved after 5 to 15 cycles. Inert purge periods were not modelled explicitly here; it was assumed that the state of the solid did not change during these periods (sample calculations demonstrating the appropriateness of this can be found in SI Section 3).

3.4. Reactor model without axial dispersion

A simplified model with a further assumption of no axial dispersion in the reactor was also implemented to compare the results with the model above. This assumption changed the governing equations to,

$$(1 - \varepsilon) \hat{\rho}_s \frac{d\delta}{dP_{O_2}^*} \left(-\frac{2}{K_c^2} \frac{y_c}{y_{CO}^2} \left(\frac{y_c}{y_{CO}} - 1 \right) \right) \frac{\partial y_{CO}}{\partial t} = u \frac{\partial y_{CO}}{\partial z} + \varepsilon \hat{\rho}_g \frac{\partial y_{CO}}{\partial t} \quad (22)$$

and

$$(1 - \varepsilon) \hat{\rho}_s \frac{d\delta}{dP_{O_2}^*} \left(2K_H \frac{y_{H_2O}}{y_H} \right) \frac{\partial y_{H_2O}}{\partial t} = u \frac{\partial y_{H_2O}}{\partial z} + \varepsilon \hat{\rho}_g \frac{\partial y_{H_2O}}{\partial t} \quad (23)$$

Without axial dispersion, the carbon and hydrogen balance $y_{CO_2} + y_{CO} = y_c$ and $y_{H_2} + y_{H_2O} = y_H$ are constant at any given location and time. This fact, together with the lack of the dispersion terms in the governing equations, reduced the computational time of the model significantly.

3.5. Gas mixing outside the reactor

In addition, to account for gas mixing in the flow system downstream of the reactor, calibration gases (5% of H_2 , H_2O , CO and CO_2 balanced in Ar, respectively) were fed to the flow system (bypassing the reactor) for a fixed period of time (approximately 30 min) to obtain the response of the system to a ‘‘Top-hat’’ input. The impulse responses for H_2 , H_2O , CO and CO_2 was estimated by de-convolving the input signal for each gas from the respective outputs using the method of conjugate gradients. The impulse responses were then convolved with the calculated outlet gas profiles to produce the final results.

4. Results

4.1. Stability of the OCM under cycling

When used industrially, it is important that the OCM is stable over repeated cycles so that it does not need to be replaced frequently. Additionally, to validate the numerical model, it is important to ensure that the OCM does not degrade significantly during repeated cycling over the duration of each experiment (60 to 1000 cycles) – although it would be possible to model such degradation if it existed, by introducing an empirical decay parameter.

In order to test the long-term stability of the OCM for the chemical-looping water–gas shift reaction, fresh $La_{0.6}Sr_{0.4}FeO_{3-\delta}$ was subjected to 1100 cycles of redox reactions with 5% CO and 5% H_2O in the horizontal packed bed system following the protocol detailed in the experimental section.

Fig. 2 shows how the conversions evolved with cycle number. The overall conversion of H_2O increased from a very low initial value in Cycle 1 to a steady value of 92.39% in Cycle 25; this value remained constant within a standard error of 0.03% for the remainder of the experiment. In contrast, the CO was almost completely converted in the first few cycles of the experiment before reaching a steady-cycling value of 84.50% within a small number of cycles (Cycles 10–15). The difference in the steady cycling conversion of CO and H_2O was due to the slightly different flowrates of the H_2O and CO used experimentally with the H_2O feed having a molar flowrate 1.05 times that of the CO feed. Once this was taken into account, the oxygen balance in the gas streams closed to within 2%.

The different initial conversions for CO and H_2O are because the OCM was initially in equilibrium with air following its synthesis, so that in the first few cycles CO could be fully converted to CO_2 due to the high oxidising potential of the solid but the subsequent H_2O stream does not return the OCM to that more oxidised state. As more of the OCM in the reactor was gradually reduced to a P_{O_2} that is suitable for H_2 production (10^{-23} to 10^{-8} bar), the conversion of H_2O to H_2 gradually increased. Once the bed no longer contains any OCM with oxygen potentials above that of the H_2O stream the CO conversion drops to match that of the H_2O ; here this process took 50 cycles.

A linear regression on conversion against cycle number over the steady cycling regime showed a gradient that was less than the standard error from the regression, suggesting that there was no measurable change in conversion over cycling.

The changes in outlet gas composition as the bed approached steady cycling can be seen in Fig. 3A-3D. Here reduction refers to bed reduction

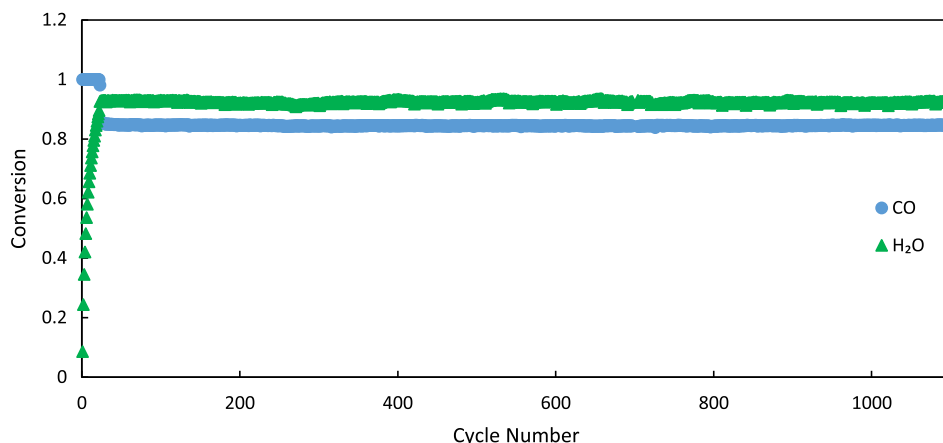


Fig. 2. Conversion versus cycle number for 1100 cycles-H₂O (green triangles) and CO (blue dots) conversion as a function of cycle number with 60 s feeds of 5 mol% CO and 5 mol% H₂O. The horizontal bed consisted of 2.79 g of 80–160 μm La_{0.6}Sr_{0.4}FeO_{3- δ} and a nominal molar feed rate of $3.4 \times 10^{-5} \text{ mol s}^{-1}$. (For interpretation of the references to colour in this figure legend, the reader is referred to the web version of this article.)

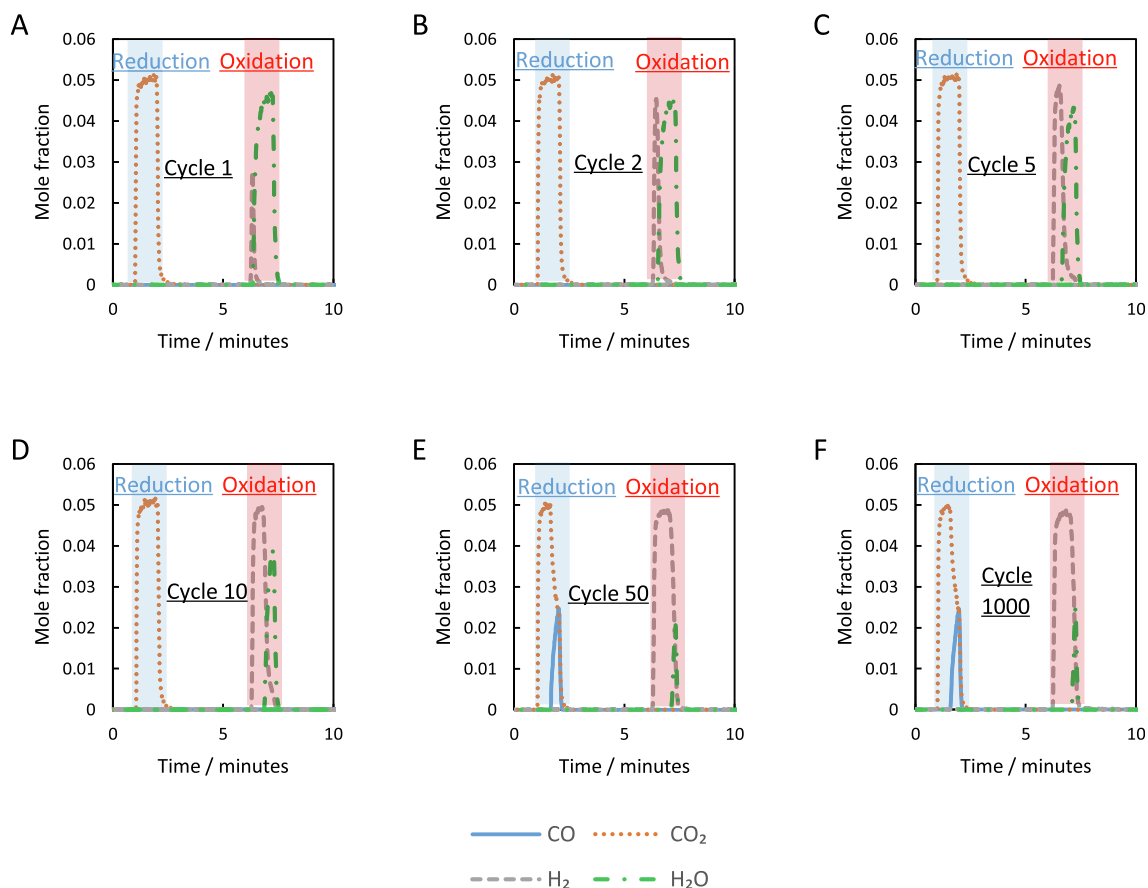


Fig. 3. Outlet composition versus time from the long-term stability experiment. Six oxidation and reduction cycles indicating the evolution of the bed into a steady-cycling regime; The uncertainty in the measured mole fraction was less than ± 100 ppm.

as CO is flowed and oxidation to bed oxidation as H₂O is flowed. Once steady cycling had occurred (Fig. 3E and F) the reduction half cycle, consisting of 5 mol% CO fed to the reactor, started with almost 100% conversion for the first 40 s before dropping gradually to a final value of 50% at 60 s. The oxidation half cycle, consisting of 5 mol% H₂O fed to the reactor, followed the same pattern, with almost pure H₂ production before a small amount of H₂O broke through. Comparing Fig. 3E and F, it can be seen that the outlet gas profile recorded during steady cycling is almost indistinguishable over multiple cycles.

Samples of the OCM were taken and examined by SEM and XRD to investigate if any significant structural changes and/or phase segregation had occurred. These showed minimal changes to both crystal structure and appearance of the sample. These results can be found in SI Section 4.

These results show that a chemical-looping water-gas shift reactor using La_{0.6}Sr_{0.4}FeO_{3- δ} can perform at very high gas phase conversions (84.5% for H₂O and 92.4% for CO) for multiple cycles with inherent CO₂ separation. The repeated cycling of the material between oxidised and

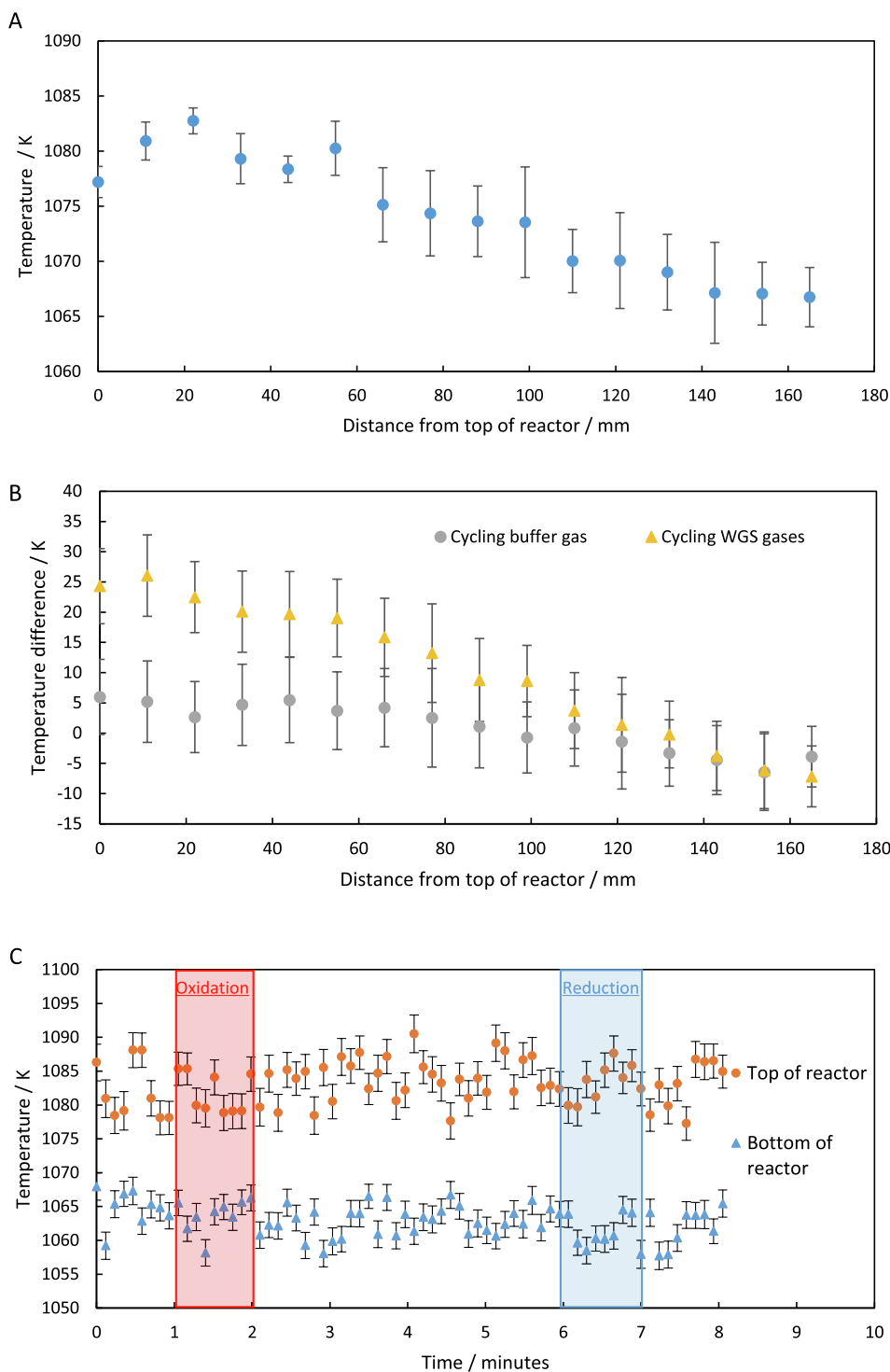


Fig. 4. A (top), time averaged temperature, calculated using the Rietveld fitting of the Y_2O_3 , as a function of position in the vertical reactor with no reaction. B (middle), the difference between the time-averaged (70 data points) temperature measurement during cycling between 5% CO and 5% H_2O in Ar (yellow triangles) and between 1:10 and 1:1 $CO_2:CO$ buffer gas feeds (grey circles) and with no reaction (seen in A). C (bottom), temperature of the ends of the reactor as a function of time over a cycle of 1-minute feeds of 5% CO and 5% H_2O in Ar. Oxidation and reduction periods have been marked. The error bars shown in 3A and 3B are the standard error based the average of 70 measurements at the same location, whereas the error bars in 3C are estimated standard error from individual Rietveld fitting. (For interpretation of the references to colour in this figure legend, the reader is referred to the web version of this article.)

reduced states does not seem to have a measurable effect on the structure of the OCM.

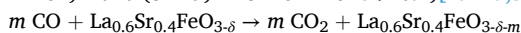
There is also no evidence of carbon deposition in the reactor during the reaction. The cumulative amount of carbon measured in the outlet gases during the reduction half cycle ($9.9 \pm 0.3 \times 10^{-5}$ mol) was within the uncertainty of that entering the reactor ($10.2 \pm 0.5 \times 10^{-5}$ mol). This is further confirmed by the absence of carbon containing species (either CO or CO_2) during the oxidation half cycle.

4.2. Temperature profile within the reactor

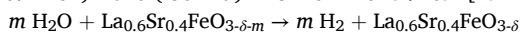
The validity of the assumption of an isothermal reactor was tested by *operando* SXR D experiments through the Rietveld fitting of the Y_2O_3 present in a packed bed of 2.2 g of $La_{0.6}Sr_{0.4}FeO_{3-\delta}$ in the size fraction 80–160 μm and 0.4 g Y_2O_3 powder sieved to less than 40 μm packed into a quartz reactor with an inner diameter of 4 mm. This resulted in a bed height of 170 mm that was cycled between different oxidising and reducing gases.

As seen from Fig. 4A, a temperature difference of approximately 16 K was measured across the reactor under inert conditions. This is primarily

due to the degree of insulating material of the furnace along the length of the reactor to enable *operando* SXRD measurements. A fully insulated furnace would produce a much smaller temperature gradient and if it was oriented horizontally the temperature profile would be symmetrical about the middle of the furnace. Fig. 4B shows the change in the temperature of the solids during cyclic operation compared to under inert conditions. When CO/CO₂ buffer gases were used, no significant temperature change was observed. This is due to the enthalpy change for the reduction of La_{0.6}Sr_{0.4}FeO_{3-δ} (Eq. (2), reproduced here) being within two standard deviations of zero when $\delta > 0.2$ (literature values vary between (-72 ± 61) m and (5 ± 9) m kJ mol⁻¹ for $\delta > 0.2$) [17–19,36].



On the other hand, when 5% H₂O was used, the top end of reactor (the H₂O inlet) increased in temperature due to the exothermic nature of the oxidation of La_{0.6}Sr_{0.4}FeO_{3-δ} by H₂O Eq. (3), found to be between (-107 ± 61) m and (-50 ± 9) m kJ mol⁻¹ for $\delta > 0.2$ [17–19,36].



Interestingly, during each cycle there is no significant temporal change in temperature once steady cycling is achieved, as seen in Fig. 4C. Frequency analysis carried out on the temperature data to determine the

presence of periodic oscillation showed that the data was dominated by the frequency of the temperature measurement. This indicates that the gas change has a much smaller effect on the temperature than random errors in the temperature measurement. The preheating of the gas stream carried out by the furnace prior to contact with the reactive solid and the comparatively small magnitude of the enthalpy change of reaction mean that the heat losses during purges happen too slowly to be accurately measured given the uncertainty in the data.

While the Rietveld fitting gives a relatively low uncertainty for any individual temperature measurement (~ 2.5 K), when the temperature from successive measurements at a given point in the reactor is averaged over a cycle (e.g. as is performed in Fig. 4A and 4B), the greater degree of scatter of data led to the standard deviation of the average temperature being 8.2 K. While relatively large, this is still less than 1% of the measured value and furnace set point. The large uncertainties associated with the average temperature measurement prevent an accurate temperature profile to be applied in the numerical model. The modelling error is constant and consistent across the investigated cycles due to the steady temperature profile. Hence, the isothermal assumption has been used in this work for simplicity. The effect of temperature on reactor

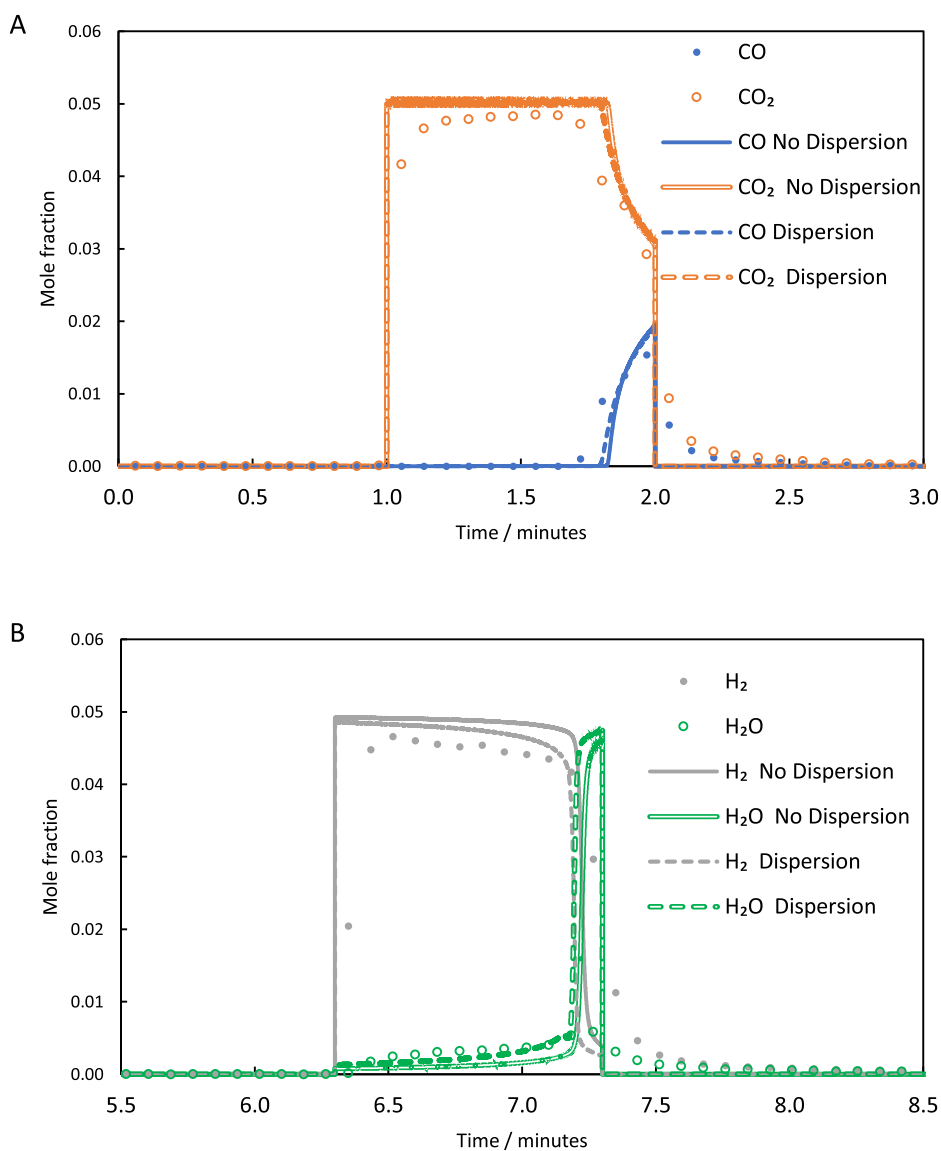


Fig. 5. Measured (dots) and simulated with (dashed lines) and without dispersion (solid lines) outlet gas mole fractions versus time for a representative steady cycle using 5% CO in Ar and 5% H₂O in Ar as the reactive gases. A and B show the comparison of experimental data, and the simulated results for the reduction half cycle and the oxidation half cycle, respectively. The uncertainty in the measured mole fraction was less than ± 100 ppm.

performance is explored later in this work using the horizontal reactor, where the temperature gradient across the reactor is smaller.

4.3. Model validation

4.3.1. Effect of axial dispersion

To test the appropriateness of the simulation scheme, the bed studied in Fig. 4 was cycled between different oxidising and reducing gases.

Fig. 5 shows the experimental and modelled outlet gas mole fraction as a function of time during steady cycling operation. It is clear from Fig. 5 that both numerical simulations, with or without axial dispersion, are in good agreement with experimental results. The inclusion of axial dispersion has limited impact on the reduction half cycle but leads to slightly better agreement with the measured mole fractions of H₂O and H₂ during the oxidation half cycle. This is due to H₂ having a much higher axial dispersion coefficient than the other species. However, the dispersion model required approximately 20 times longer to compute than the model without axial dispersion, and the marginal improvement of the simulation results does not justify the increase in computational cost. Thus, the dispersion terms were omitted in subsequent work of this study. In systems with lower flowrates and a longer more tortuous path for the gas through the reactor it may become necessary to model the dispersion, as it would have a larger effect on the outlet gas composition.

It is worth noting that the mole fractions of the products and reactants measured here (and all other experiments from this study) deviated from plug flow behaviour (*Pe* numbers between 1.28 for H₂ and 6.53 for CO₂). With suitably slow flows the effect of diffusion would

increase, back flow of different species in the mixture would be more significant with the rise and drop in each gas being slower. However, as a practical reactor would not be operated in such a way the omission is justified.

4.3.2. Effect of the response of the mass spectrometer

In order to examine whether mixing in the flow system downstream of the reactor is responsible for the mismatch between simulated and measured results, the outlet gas conditions shown in Fig. 5 of the dispersion-free results were convolved with the impulse response of the same apparatus, for each gas species, including the mass spectrometer but with the reactor bypassed. The results are shown in Fig. 6. As expected, convolution smooths and changes the shapes of the curves. For the CO half cycle this brings the simulated results closer to those measured experimentally, improving the shape of the increase of the mole fraction of gases at the beginning and middle of the cycle, however the decrease in CO₂ mole fraction towards the end of the cycle deviates further from the measurements. The convolution added the tails to the model prediction, but the predicted rate of decay was still faster than that seen in the experiment.

For the oxidation half cycle the addition of the convolution smoothed the initial increase in H₂ mole fraction as well as adding the tails at the end of the cycle. However, the convolution failed to address the under prediction of the H₂O content For the first 40 s of the oxidation half cycle.

Overall, accounting for gas mixing using convolution did not improve the simulation results substantially. The deviations may be due to other factors such as the reactions being partly limited by reactions kinetics,

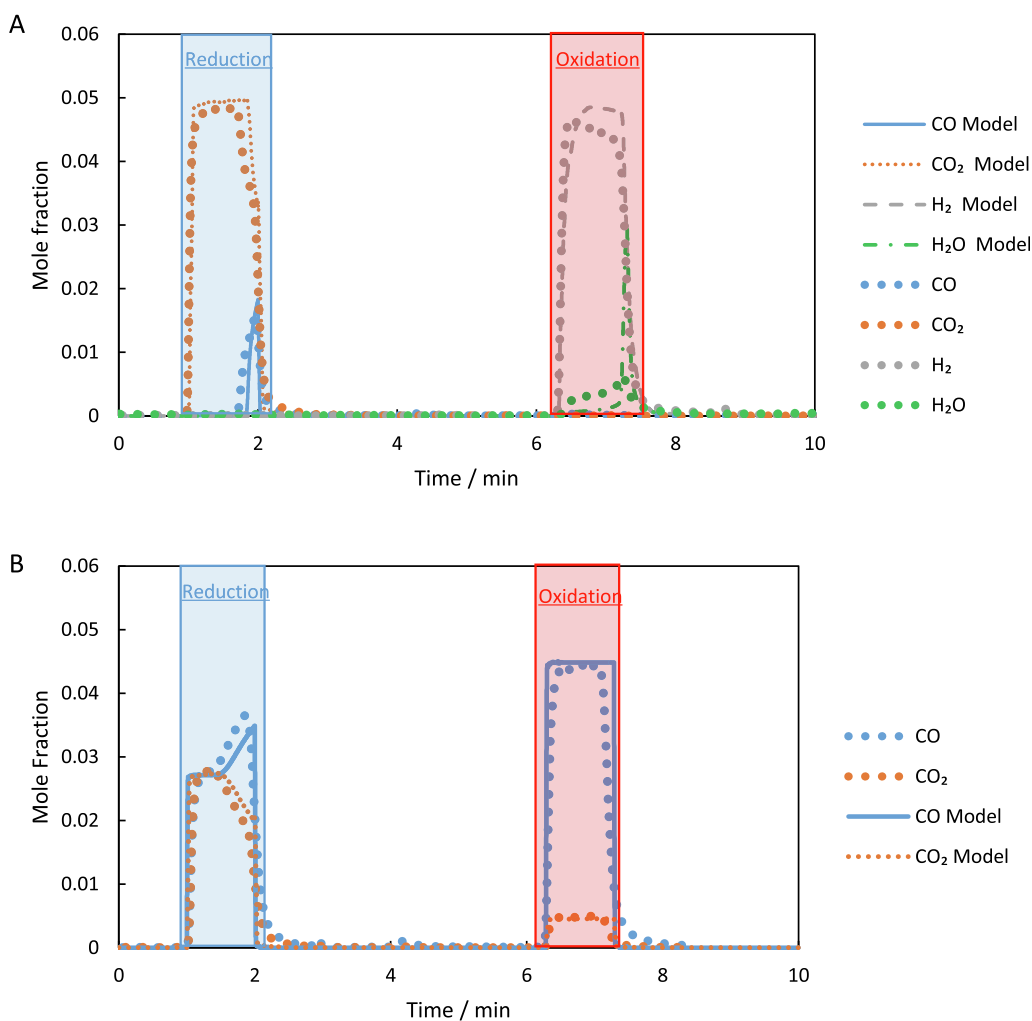


Fig. 6. Outlet gas mole fractions as a function of time for a representative steady state cycle for a reverse-flow reactor being fed A) 5% CO in Ar and 5% H₂O in Ar or B) 5% CO with 0.5% CO₂ and 2.5% CO with 2.5% CO₂ with inert purge in-between. The bed was the same as used in the previous figures. The solid lines are the values predicted by the simulation of the bed convolved with the system's impulse response, while the points are experimental measurements. The uncertainties in the measured mole fractions were less than ± 100 ppm.

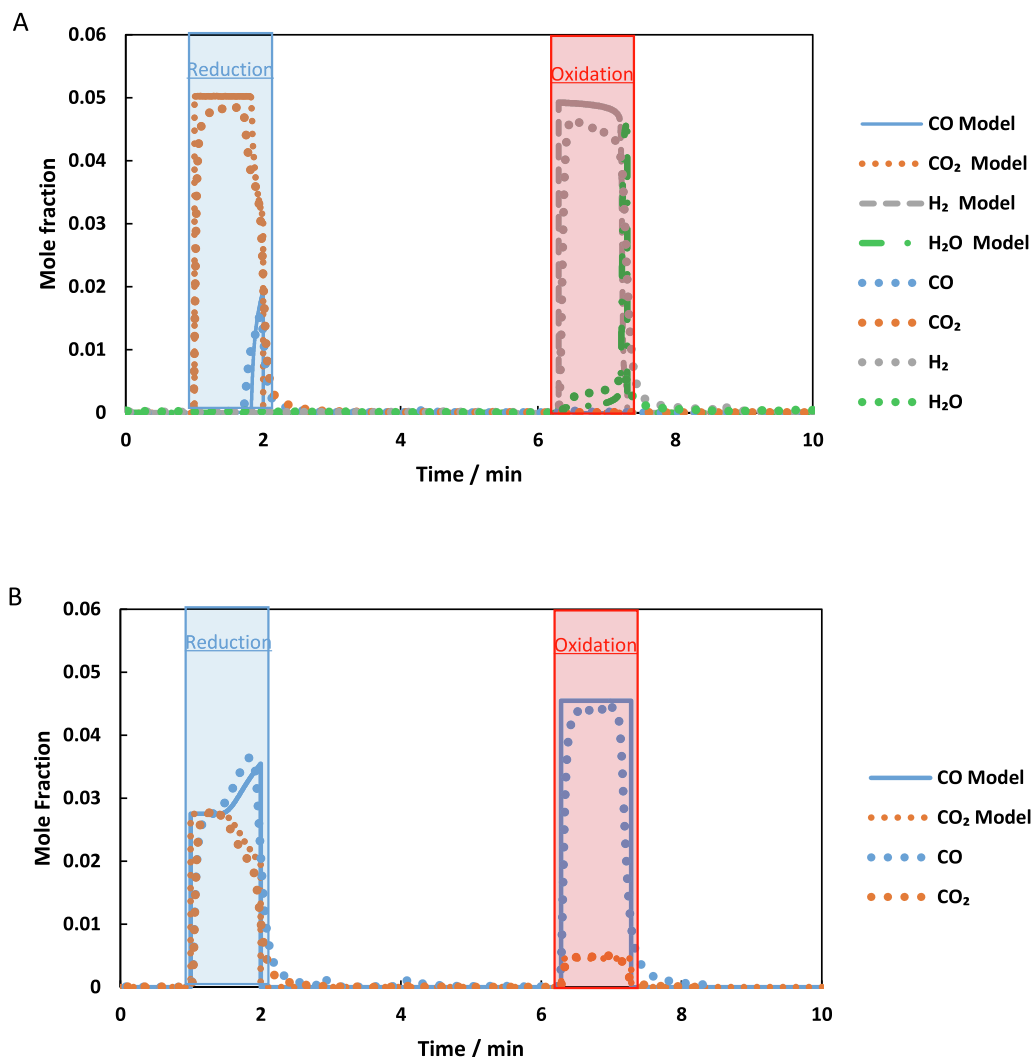


Fig. 7. Outlet gas mole fractions versus time for a representative steady state cycle for a reverse-flow reactor being fed with A: 5% CO in Ar and 5% H₂O in Ar or B: 5% CO with 0.5% CO₂ and 2.5% CO with 2.5% CO₂.

dispersion of reactive gases before entering the reactor and/or interphase mass transfer resistances. However, the overall reactor behaviour is well captured by the model, and it is possible to use it for semi-quantitative analysis of the reactor system.

4.3.3. Gas phase composition

Using the model without axial dispersion, it is possible to predict the expected outlet gas concentrations as a function of time with reasonable accuracy. These are compared to experimental results to validate the assumption that the system is thermodynamically limited. As the activity of the OCM did not change over prolonged operation, the study focuses on the comparison between the simulated gas concentration profiles at the outlet of the reactor and those measured from a representative cycle once steady cycling was achieved.

The measured outlet gas concentration profiles from the chemical-looping water-gas shift reaction, Fig. 7A, show that full conversion of CO to CO₂ was achieved for most of the reduction half cycle (between $t = 1$ and 2 min) and breakthrough of CO was seen approximately 10 s before the end of the half cycle. In contrast, during the oxidation half cycle (starting around $t = 6.3$ min) H₂O was always present at low levels and no “breakthrough” was observed. Over the course of the half cycle, the H₂ mole fraction decreased steadily and the H₂O content increased accordingly, so that the combined mole fraction of H₂O and H₂ averaged over a cycle remained constant at 0.05.

When redox buffers were used as the reactive gases (CO₂:CO ratio of 1:10 for the reducing stream and 1:1 for the oxidising stream), the results were qualitatively similar to the water-gas shift case. As shown in Fig. 7B, the reducing stream with CO₂:CO = 1:10 was initially converted to a 1:1 ratio (i.e. “full” conversion to the same oxygen potential as the oxidising stream used) but over the cycle the conversion decreased with more CO passing through the reactor unreacted. In contrast, the oxidising stream was “fully” converted throughout the oxidising cycle: a stream of CO₂:CO = 1:10 was obtained at the outlet, the same as the inlet condition of the reducing half cycle. The difference in the oxygen capacity of the gas streams accounts for the oxidation and reduction half cycles behaving more asymmetrically than the water-gas shift case: a material balance shows that the reducing stream can accept twice as much oxygen as an oxidising stream (CO₂:CO = 1:1) with the same flowrate is capable of donating.

The simulated mole fraction profiles of the products and reactants as a function of time agree well with the experiments. For instance, the time at which the conversion of CO to CO₂ started to decrease was closely captured by the model, as was how the outlet gas composition as a function of time changed with the replacement of the feeds with buffer gases. The times at which the conversion of CO or H₂O start to decrease are key parameters for controlling a scaled-up reactor, so being able to accurately predict them using modelling will allow for easier plant design and operational control.

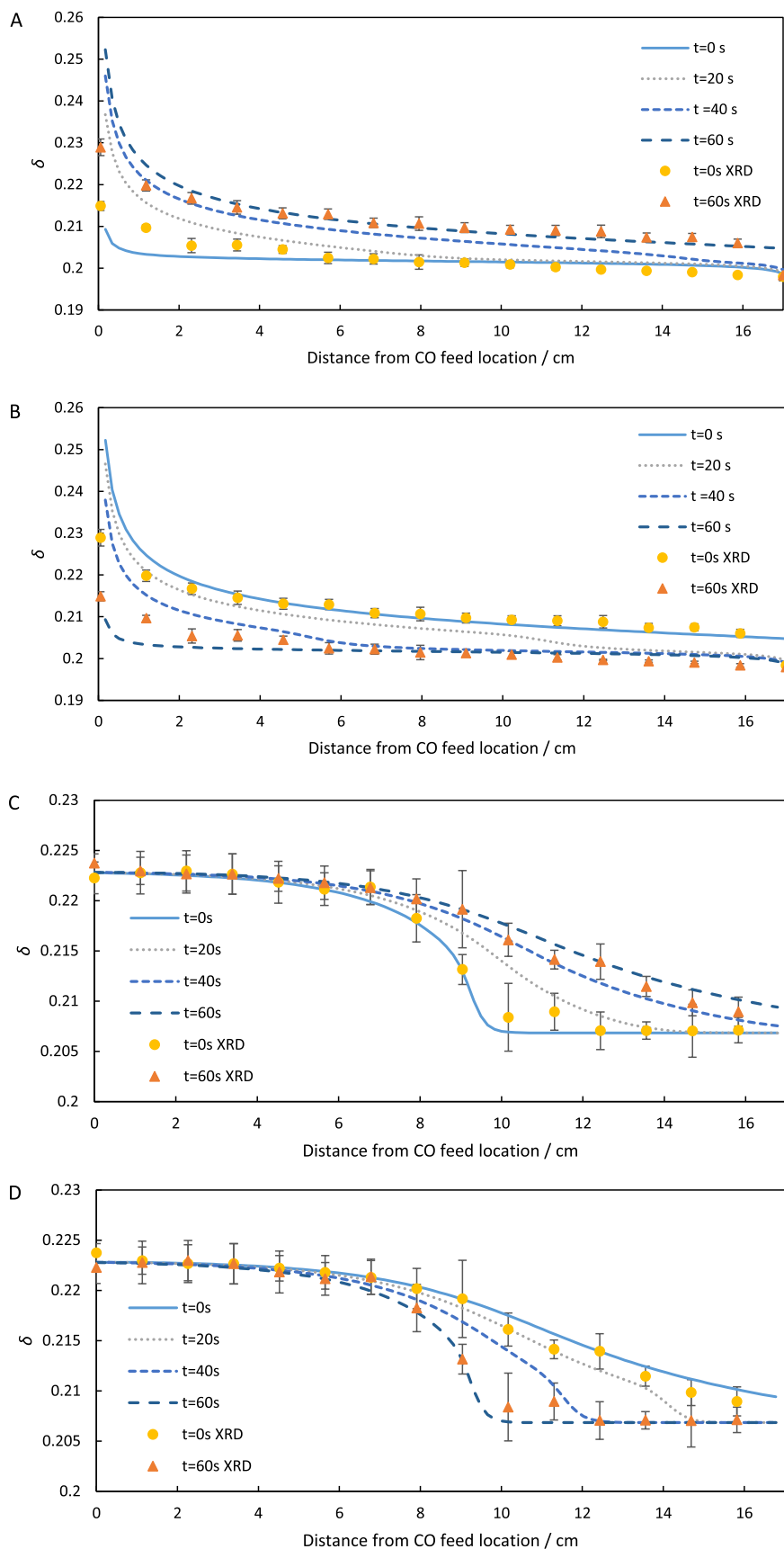


Fig. 8. δ of the bed at 20 s increments simulated using a thermodynamically limited model for a 60 s feed of A) 5% CO in Ar, B) 5% H₂O to a bed, C) 2.5% CO₂ and 2.5% CO in Ar or D) 5% CO₂ and 0.5% CO in Ar that had reached steady cycling as measured using *operando* SXR. An uncertainty of one standard deviation is plotted on the experimental data.

4.3.4. Variation of δ in the $\text{La}_{0.6}\text{Sr}_{0.4}\text{FeO}_{3-\delta}$ bed

The thermodynamic model also predicts the spatiotemporal variation of δ in the $\text{La}_{0.6}\text{Sr}_{0.4}\text{FeO}_{3-\delta}$ bed under steady cyclic operation, where δ at the beginning and end of the cycle at any given point in space is the same. Snapshots of the expected δ during the reduction and oxidation half cycles of the chemical-looping water–gas shift can be seen in Fig. 8A and B, while the corresponding results from buffer gas cycling are shown in Fig. 8C and D, respectively. These are compared to the measured variations in δ along the packed bed (obtained from *operando* SXR D using the technique detailed by de Leeuwe *et al* [20,25]) at the beginning and end of each half cycle.

For the chemical-looping water–gas shift experiment, shown in Fig. 8A and B, the reaction started with the CO feeding from the bottom of the reactor (or left of Fig. 8). The bed material near the inlet reduced first (δ increased) while the rest of the bed remained unchanged. The front of the reduction shifted gradually towards the outlet whilst the material behind the front continued to be reduced further. After 60 s, the flow of CO was stopped and H_2O was fed in the reverse direction, pushing the reduced front back through the bed, as well as lowering the δ of the bed as a whole. This continued until the bed returned to its original state.

The simulated results reproduce the experimental extent of oxidation and reduction at the oxidised end of the bed well but underestimate the extent of the reduction of material exposed to the most reducing conditions (i.e. towards the left of Fig. 8A and B). This can be attributed to the fact that for $\delta \lesssim 0.23$, $\text{La}_{0.6}\text{Sr}_{0.4}\text{FeO}_{3-\delta}$ is known to undergo rapid oxygen loss. However beyond this range it becomes unstable and undergoes slow decomposition. Since the decomposition reaction is kinetically limited, the model no longer holds. This also accounts for the better agreement between model and experimental results seen in Fig. 8C and D as the gases involved are less reducing.

In terms of oxygen balance across a half cycle, the model predicted that the packed bed containing 0.01 mol (or 2.2 g) $\text{La}_{0.6}\text{Sr}_{0.4}\text{FeO}_{3-\delta}$ lost 8.9×10^{-5} mol of oxygen during reduction, all of which were regained during the oxidation half cycle. This was compared to the experimental oxygen exchanged measured using the X-ray diffraction and outlet gas compositions. Both these methods showed similar amount of oxygen being exchanged in each half cycle. SXR D showed $9.0 \pm 0.5 \times 10^{-5}$ mol and the gas analysis gave $9.5 \pm 0.3 \times 10^{-5}$ mol. All three values agreed to within 6%.

The same analysis was carried out on the experiment using buffer gas feeds and is shown in Fig. 8C and D. This gives similar results with a

reaction front propagating through the bed. Here, however, the lower capacity for oxygen exchange of the oxidising gas resulted in changes of the OCM only in half of the bed. The model predicted 4.2×10^{-5} mol of oxygen transferred between the gas and the solid in each half cycle, while SXR D showed $3.0 \pm 0.5 \times 10^{-5}$ mol and the gas analysis $3.6 \pm 0.3 \times 10^{-5}$ mol. The results are in reasonable agreement, given that the reaction had a lower amount of oxygen transferred and smaller changes in δ compared to the previous case while the measuring precision of the lattice parameter or gas mole fractions remained the same.

While undergoing cycling, it can be seen that for both the chemical-looping water–gas shift reaction (Fig. 9A) and the reaction with buffer gases (Fig. 9B), the variation of δ at one point in the bed as a function of time during reduction is not simply the reverse of that during oxidation. However, the value of δ does return to the starting conditions after a full cycle. Unfortunately, it was only possible to collect 10 data points during each reactive period, and the changes in the cubic cell parameter during these periods are near the limit of precision of the equipment, of the order of 10^{-4} Å. As a result, while the experimental data are consistent with this aspect of the model, the uncertainties (shown in Fig. 9) are too large to validate it quantitatively. Fig. 10.

4.4. Effect of temperature on reactor performance

Simulations and experiments were also performed to examine the effect of temperature on the performance of the packed bed chemical-looping reactor. A horizontal packed bed consisting of 2.39 g of 80–160 μm $\text{La}_{0.6}\text{Sr}_{0.4}\text{FeO}_{3-\delta}$ was cycled between 5% CO and 5% H_2O until steady cycling was reached at five temperatures, ranging from 993 K to 1193 K. The outlet gas compositions were compared to those predicted by the model. The geometry of this packed bed was different to those used in the previous section, it was a shorter reactor bed with a larger internal diameter.

Both the model results and the experimentally measured gas compositions from the outlet of the reactor during the reduction half cycle started with effectively full conversion of CO to CO_2 and breakthrough of CO was observed later in the half cycle. At higher temperatures, the breakthrough of the CO occurred later, and the conversion of CO increased accordingly. A different behaviour was observed for the oxidation half cycle. At higher temperatures H_2O passes through the reactor unreacted from the start of the half cycle, the proportion of which increased with temperature. As the reaction proceeded, the

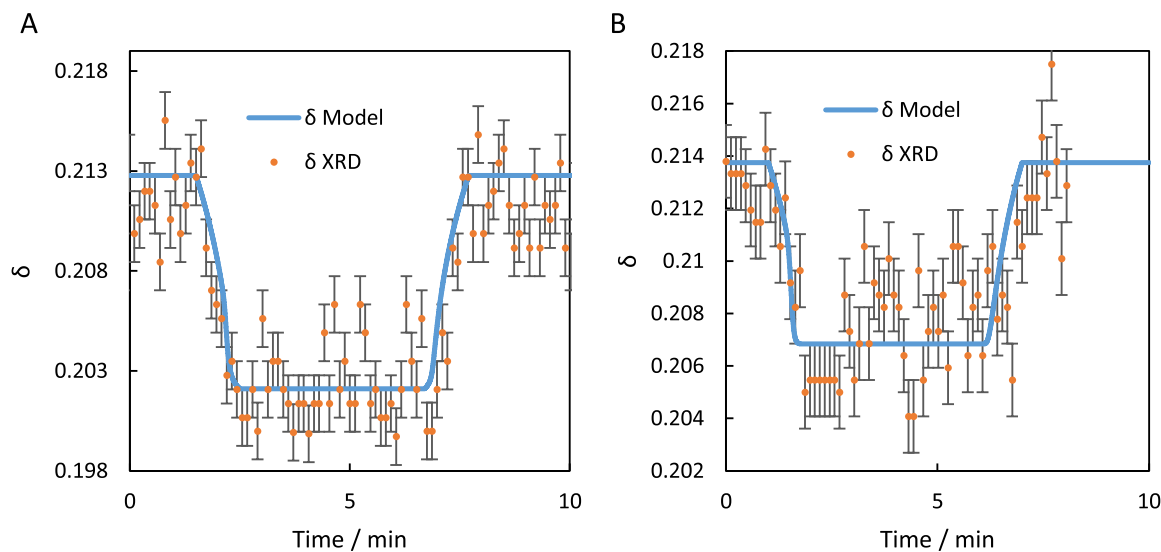


Fig. 9. δ at one point in the bed, A) 40 mm from the H_2O feed, versus time for a representative steady cycle, for a reverse-flow reactor being fed 5% CO in Ar and 5% H_2O in Ar with inert feeds in-between; B) 128 mm from the oxidising feed, for a representative steady cycle of the packed bed from Fig. 4. The solid line is the value predicted by the simulation while the points are the values obtained from SXR D. The error bars are one standard deviation from the Rietveld fitting.

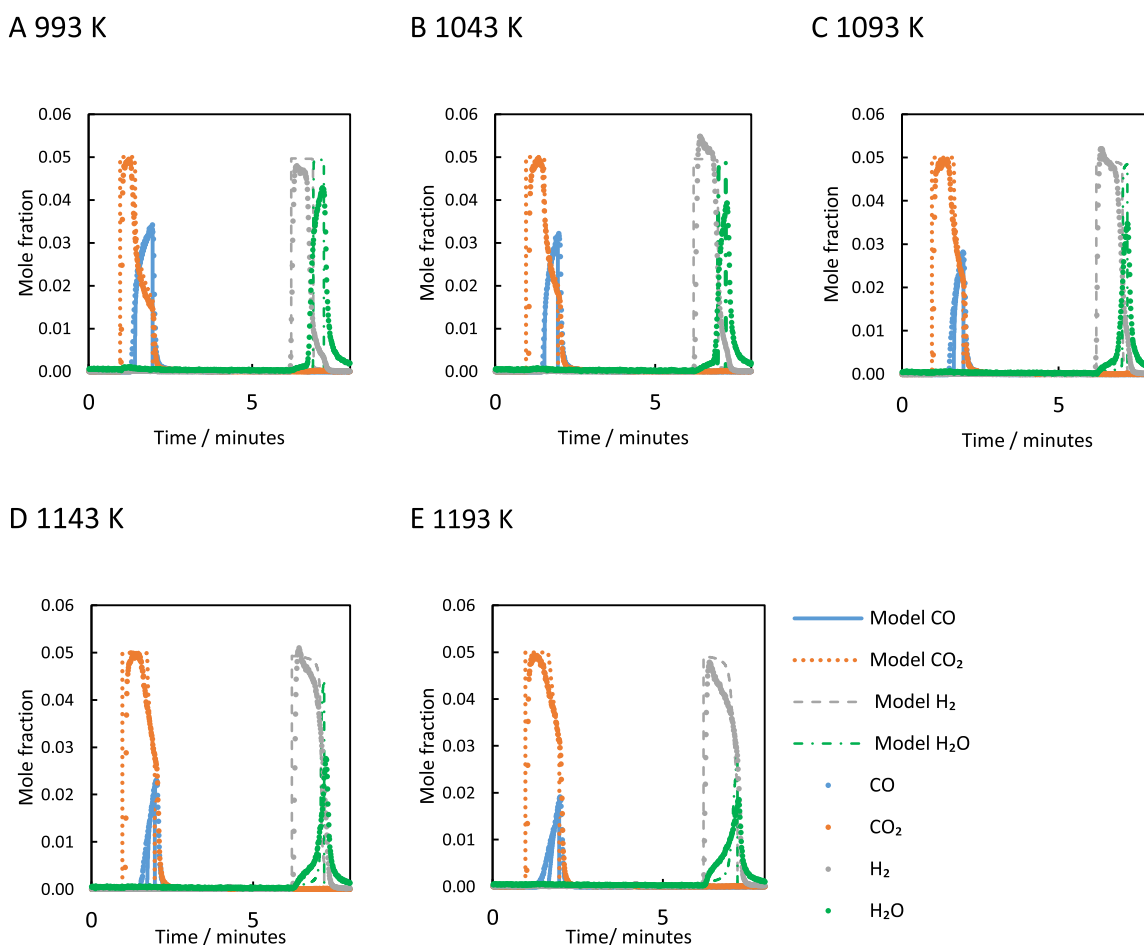


Fig. 10. Outlet composition versus time at different operating temperatures with an OCM mass of 2.39 g. The feed gases 5% CO and 5% H₂O in a balance of Ar, respectively, with nominal molar flowrates of $3.4 \times 10^{-5} \text{ mol s}^{-1}$. The packed bed had an internal diameter of 0.007 m and a length of 0.06 m. The uncertainties in the measured mole fractions were less than ± 100 ppm.

proportion of H₂O in the product increased continuously, but the rate of this increase decreased with temperature and the overall conversion of H₂O to H₂ increased with temperature. These changes can be predicted by our model in spite of the different geometry and temperatures used, showing that the model is generally applicable for small-scale packed bed reactors. It should also be noted that any H₂O present in the H₂ stream can be easily separated through condensation.

Comparison between the simulated and experimental results shows that the model consistently slightly over-predicts product concentrations at a maximum of 0.2 mol% at any given point and under-predicts reactant concentration in the product streams at all temperatures studied by the same amount. However, the timing of the drop in CO₂ and H₂ mole fractions in the product streams can be predicted accurately. This shows that the reactor continues to operate near (but probably not at) its thermodynamic limit in this range of temperatures.

5. Discussion

5.1. Process sensitivity analysis

Process sensitivity analysis was carried out to determine the model's sensitivity to key operating parameters and different input conditions. The controlled variables were perturbed by 10% (or 10 K in the case of reaction temperature), as this is larger than the uncertainties in the set point or measuring instrument of each variable. The variation caused by each of these changes can be seen in Fig. 11.

Of the controlled variables (Fig. 11A-C), the change in the total mass of OCM has the largest impact on the results. This is expected since the

oxygen capacity of the solid scales with its mass. On the other hand, changing the pressure of the reactor while maintaining the same molar flow rate of the gas has no measurable impact on the simulations. It should be noted that this is only true when the reactor is equilibrium limited. If the residence time of the gas is too low, reaction kinetics may limit the conversion with insufficient contact time between the gas and solid. Temperature effects are also small compared to the effect of changing the mass of OCM. This is because the reduction and oxidation reactions Eqs. (2 and 3) are almost heat-neutral for La_{0.6}Sr_{0.4}FeO_{3- δ} [16], so changes in the operating temperature would only result in small shifts in the gas–solid equilibrium.

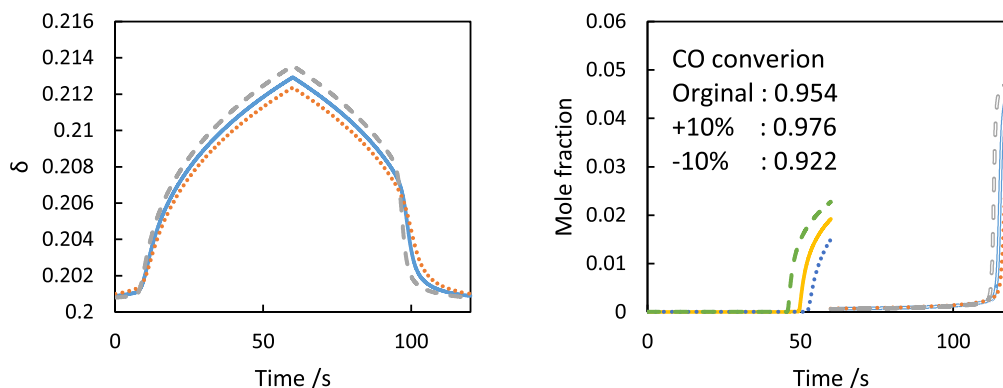
5.2. Model parameter sensitivity analysis

Model parameter sensitivity analysis was also carried out to determine the model's sensitivity to the thermodynamic quantities from the literature. Where values taken from literature have published uncertainties, the effects of a one standard deviation perturbation in that value were determined.

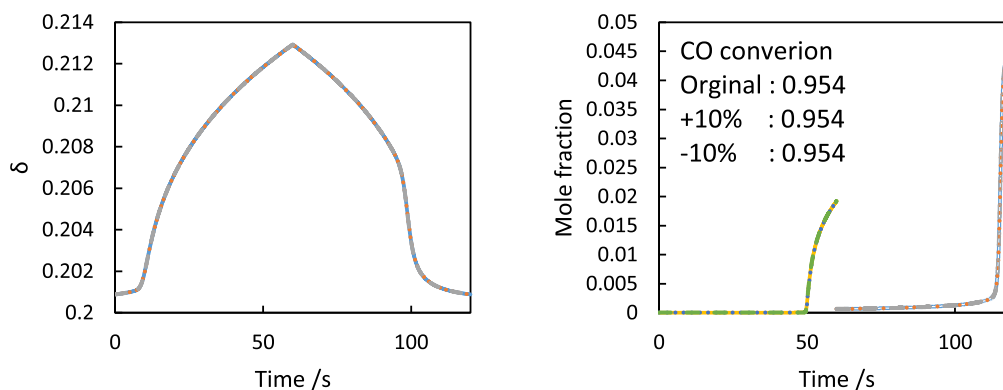
Of the thermodynamic parameters investigated (Fig. 12A-D), the uncertainty in K_{Fe} has the largest impact on the model output while K_{Ox} has a much smaller effect. This is expected as K_{Fe} relates to the reduction of Fe³⁺ to Fe²⁺, which dominates in the P_{O_2} range where the reactor operates; while K_{Ox} is linked to the oxidation of Fe³⁺ to Fe⁴⁺, which primarily occurs at higher P_{O_2} values.

The model is less sensitive to changes in the gas phase equilibrium constants (K_c and K_H from Eqs. (14 and 20), respectively). The effect of

A. The effect of varying the total mass of OCM present by 10%.



B. The effect of varying the operating pressure by 10%



C. The effect of varying the temperature of the reactor by 10 K

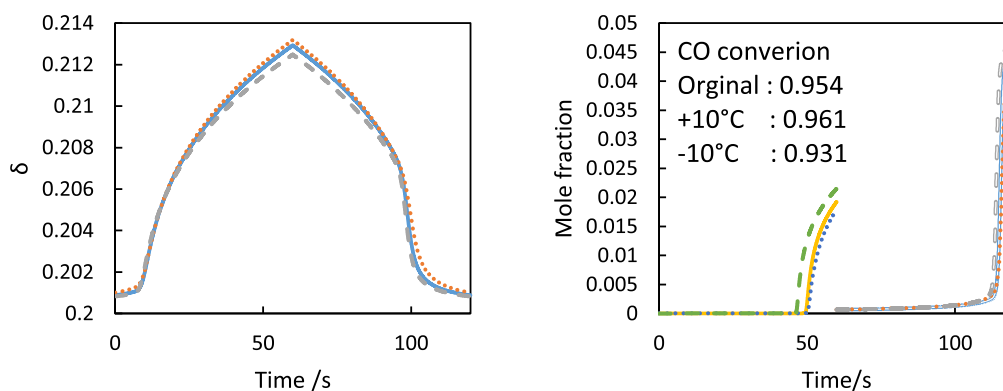
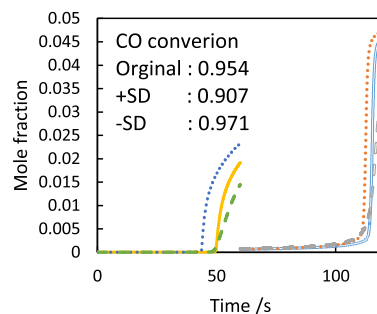
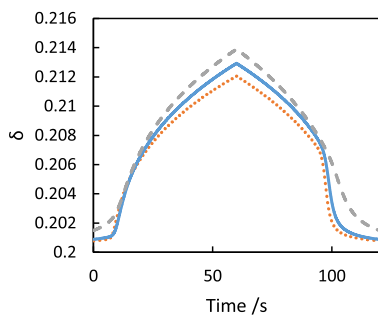
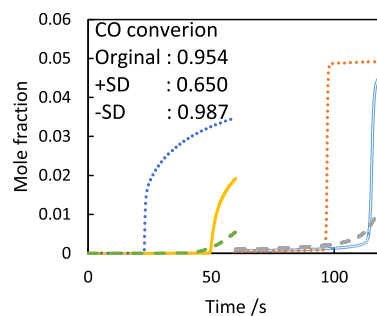
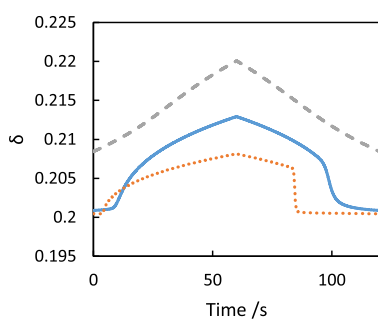


Fig. 11. Sensitivity analysis of δ at one point in the bed, 40 mm from the H₂O feed end (left) and H₂O and CO outlet gas composition (right), versus time for a steady state cycle. The base case is for a reverse-flow reactor operating at 1023 K being fed 5% CO in Ar for 60 s followed by 5% H₂O in Ar for 60 s. The bed is a 2.2 g, packed bed of La_{0.6}Sr_{0.4}FeO_{3- δ} 170 mm in length and 4 mm in diameter.

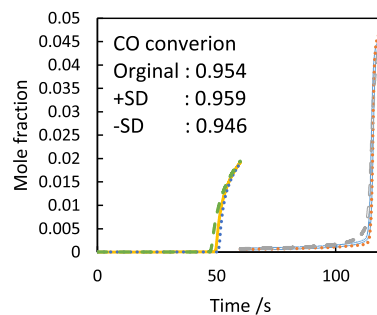
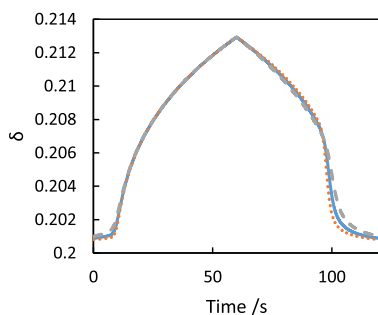
A. The effect of changing K_{Ox}



B. The effect of changing K_{Fe}



C. The effect of varying K_H



D. The effect of varying K_C

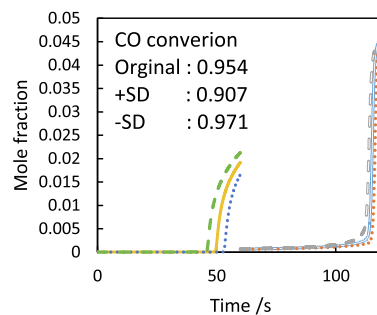
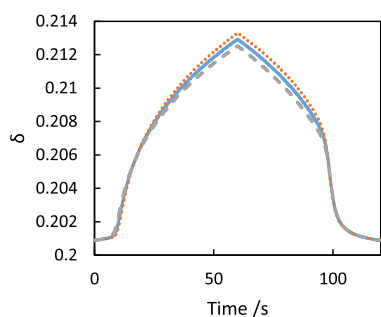


Fig. 12. Sensitivity analysis of δ at one point in the bed, 40 mm from the H₂O feed end (left) and H₂O and CO outlet gas composition (right), versus time for a steady state cycle. The base case is for a reverse-flow reactor operating at 1023 K being fed 5% CO in Ar for 60 s followed by 5% H₂O in Ar for 60 s. The bed is a 2.2 g, packed bed of La_{0.6}Sr_{0.4}FeO_{3- δ} 170 mm in length and 4 mm in diameter.

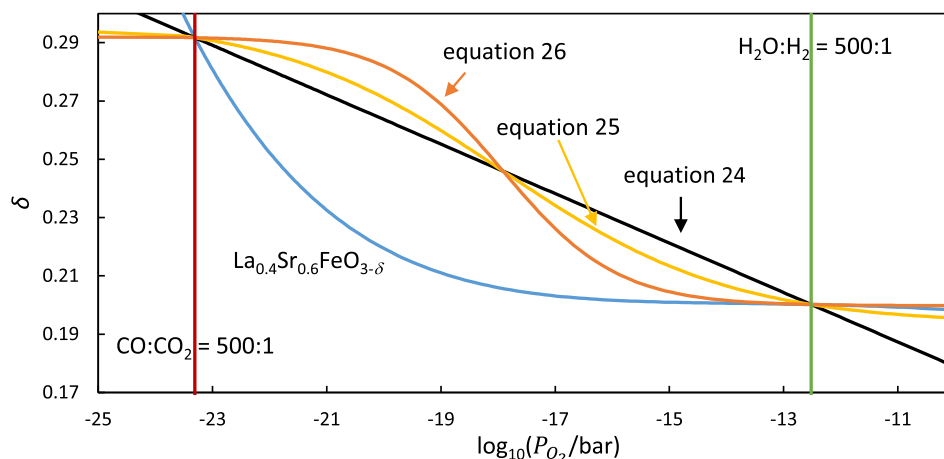


Fig. 13. δ as a function of P_{O_2} based on literature values [18] at 1093 K compared to different hypothetical relationships with rotational symmetry of order 2.

changing K_c (i.e. changing the equivalent P_{O_2} of the reducing gas) is more pronounced. This is due to the larger gradient in the δ - P_{O_2} relationship in reducing environments (Fig. 1 from the SI highlights this), so that the available oxygen capacity of the solid is more dependent on the P_{O_2} of the reducing stream than that of the oxidising stream (H_2O).

5.3. Impact of solid phase thermodynamics

From the sensitivity analysis, it is clear that the solid phase thermo-

dynamics, in particular K_{Fe} , is most influential. In addition, gas phase equilibria (K_c and K_H) of the reduction and oxidation reaction affect the model outcome differently. Both observations are linked to the δ - P_{O_2} relationship of the nonstoichiometric oxygen carrier. Here, several hypothetical δ - P_{O_2} relationships are described to demonstrate its importance further and guide future reactor design.

A series of simulations were carried out using different theoretical δ - P_{O_2} relationships with a rotational symmetry of order 2 in $\log_{10}P_{O_2}$ with

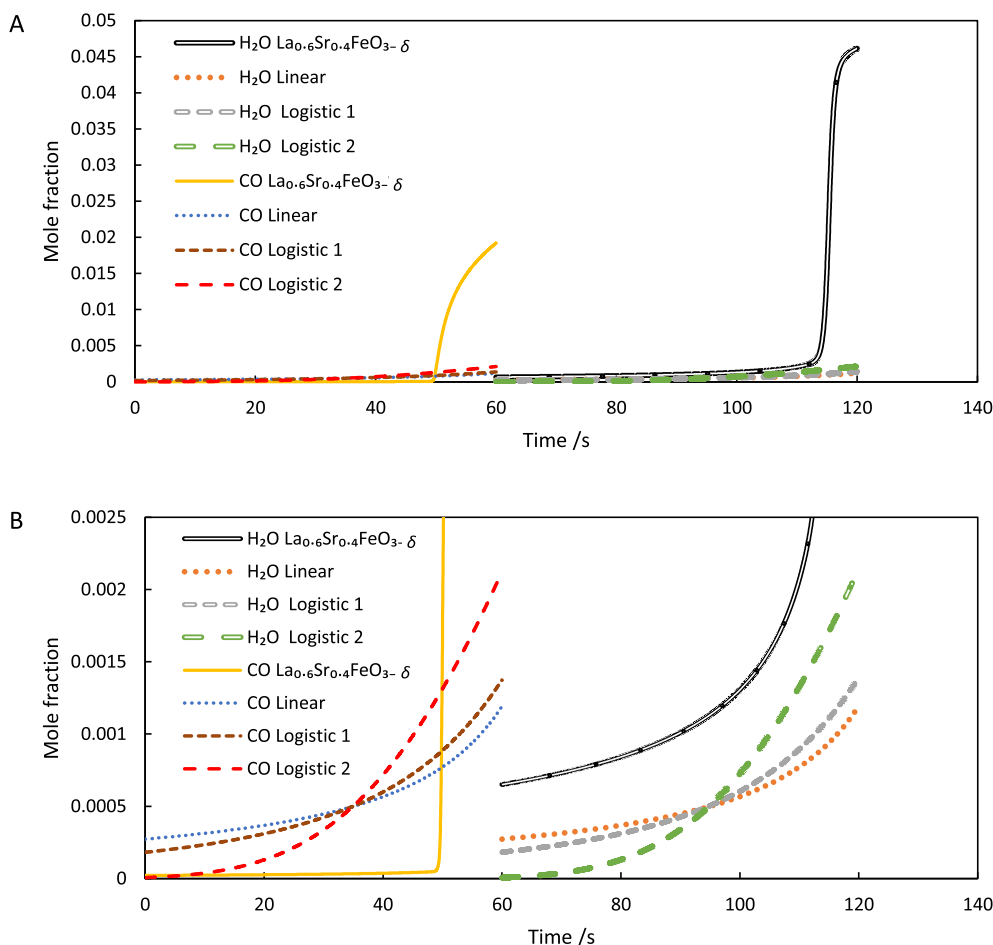


Fig. 14. H_2O and CO outlet gas compositions versus time from a steady cycle under the same operating conditions as in Fig. 5. Four different relationships between $\log_{10}P_{O_2}$ and δ state were simulated: that of $La_{0.6}Sr_{0.4}FeO_{3-\delta}$, a linear relationship (Eq. (24)) and two logistic relationships given by Eq. (25)–(26). A: full scale of gas mole fractions; B: mole fractions up to 0.0025 to show the differences between the hypothetical materials more closely.

origin $\delta = 0.246$ and $\log_{10}P_{O_2} = -17.9$ in for $-23.3 < \log_{10}P_{O_2} < -12.5$. One linear and two logistic relationships between $\log_{10}P_{O_2}$ and δ were tested. The function parameters were selected to maintain the same oxygen exchange capacity of the material over the range of P_{O_2} expected to be present in the reactor. These are detailed in Eqs. (24–26) and plotted in Fig. 13.

$$\delta = -8.48 \times 10^{-3} \times \log_{10}P_{O_2} + 0.0941 \quad (24)$$

$$\delta = \frac{-1.05 \times 10^{-1}}{1 + e^{-0.5(\log_{10}P_{O_2} + 17.9)}} + 0.298 \quad (25)$$

$$\delta = \frac{-9.242 \times 10^{-2}}{1 + e^{-(\log_{10}P_{O_2} + 17.9)}} + 0.292 \quad (26)$$

The outlet gas compositions from steady cyclic operation are shown in Fig. 14. All three hypothetical OCMs led to higher conversions of both CO and H₂O compared to La_{0.6}Sr_{0.4}FeO_{3- δ} , despite them all having the same maximum oxygen exchange capacity. All three symmetric relationships gave an overall conversion of 99% compared with 95% for La_{0.6}Sr_{0.4}FeO_{3- δ} . It is also interesting to note from Fig. 13B that the outlet gas composition profiles of the hypothetical OCMs have a common intersection when the instantaneous conversion was at 99% but the reason behind this is unclear.

In the case of La_{0.6}Sr_{0.4}FeO_{3- δ} , breakthrough of CO occurred earlier than H₂O, but a small yet appreciable amount of H₂O was present in the product stream before the breakthrough. For the hypothetical materials where the δ - $\log_{10}P_{O_2}$ relationship has rotational symmetry order 2 about $(\log_{10}P_{O_2}, \delta) = (0.246, -17.9)$, the breakthrough behaviour of CO is the same as that of H₂O. However, this is only because the equilibrium constant for the water-gas shift reaction is unity at this temperature. At other temperatures, CO/CO₂ and H₂/H₂O gas mixtures with the same ratio do not have the same P_{O_2} , so the shape of the breakthrough curves will be different.

6. Conclusions

In this work a packed-bed chemical looping water gas shift reactor with variable oxygen non-stoichiometry was described using a thermodynamic model and the model predictions compared to experimental outlet gas compositions. The internal oxygen content of the bed as a function of time and location was determined using *operando* synchrotron XRD and compared to the model. Several theoretical relationships between the oxygen content of the solid and the corresponding equilibrium P_{O_2} were also investigated based on the model developed.

It was found that such a reactor, using La_{0.6}Sr_{0.4}FeO_{3- δ} , can be effectively described using a thermodynamic model in a temperature range of 993 K to 1193 K without any fitted parameters. This is due to the fast kinetics for the gas-solid reactions and high oxygen conductivity of the solid.

It was also found that these small-scale packed bed reactors can be modelled as plug flow reactors due to the low diffusivity of the gasses involved

For a chemical looping reactor using non-stoichiometric OCMs the relationship between oxygen content and gas phase P_{O_2} is the defining feature. When an OCM with a designer relationship between oxygen content and P_{O_2} is used the response of the system can be tailored. This means that careful consideration should be placed on the selection of the optimal oxygen carrier material such that the relationship between oxygen content and gas phase P_{O_2} gives the best result

Declaration of Competing Interest

The authors declare that they have no known competing financial interests or personal relationships that could have appeared to influence the work reported in this paper.

Acknowledgments

The synchrotron experiments were performed on beamline ID22 at the European Synchrotron Radiation Facility (ESRF), Grenoble, France. We are grateful to Andy Fitch and Catherine Dejoie for providing assistance in using beamline ID22. We thank Claire Thompson for producing early drafts of Fig. 1. The research leading to these results has received funding from the European Research Council under the European Union's Seventh Framework Programme (FP/2007–2013)/ERC grant agreement no. 320725 and under Horizon 2020/ERC grant agreement no. 96151 and from the EPSRC via grants EP/P007767/1 and EP/P024807/1. CdL thanks EPSRC for funding via a doctoral training award. ISM acknowledges funding from the Royal Academy of Engineering through a Chair in Emerging Technologies award entitled "Engineering chemical reactor technologies for a low-carbon energy future," grant number CIET1819\2\57.

Data availability

Data supporting this publication are openly available under an 'Open Data Commons Open Database License'. The data, with additional metadata, are available at <https://doi.org/10.25405/data.ncl.13625906>.

Appendix A. Supplementary data

Supplementary data to this article can be found online at <https://doi.org/10.1016/j.cej.2021.130174>.

References

- [1] M. Ball, M. Weeda, The hydrogen economy - Vision or reality? Int. J. Hydrogen Energy 40 (2015) 7903–7919, <https://doi.org/10.1016/j.ijhydene.2015.04.032>.
- [2] C. Philibert, International energy agency insights series 2017, Renew. Energy Ind. (2017).
- [3] I. Dincer, C. Acar, Review and evaluation of hydrogen production methods for better sustainability, Int. J. Hydrogen Energy 40 (34) (2015) 11094–11111, <https://doi.org/10.1016/j.ijhydene.2014.12.035>.
- [4] P.D. Vaidya, A.E. Rodrigues, Insight into steam reforming of ethanol to produce hydrogen for fuel cells, Chem. Eng. J. 117 (1) (2006) 39–49, <https://doi.org/10.1016/j.cej.2005.12.008>.
- [5] S.J. Gasior, A.J. Forney, J.H. Field, D. Bienstock, H.E. Benson, Production of synthesis gas and hydrogen by the steam-iron process: pilot-plant study of fluidized and free-falling beds, Bureau of Mines (1961).
- [6] J.C. Schouten, Chemical Reaction Engineering: History, recent developments, future scope, Proc. Jahrestreffen Reaktionstechnik (2009) 3–4.
- [7] M.P. Dudukovic, Frontiers in Reactor Engineering, Science 325 (5941) (2009) 698–701, <https://doi.org/10.1126/science.1174274>.
- [8] T. Mattisson, A. Lyngfelt, P. Cho, The use of iron oxide as an oxygen carrier in chemical-looping combustion of methane with inherent separation of CO₂, Fuel 80 (13) (2001) 1953–1962, [https://doi.org/10.1016/S0016-2361\(01\)00051-5](https://doi.org/10.1016/S0016-2361(01)00051-5).
- [9] A. Thursfield, A. Murugan, R. Franca, I.S. Metcalfe, Chemical looping and oxygen permeable ceramic membranes for hydrogen production – a review, Energy Environ. Sci. 5 (6) (2012) 7421, <https://doi.org/10.1039/c2ee03470k>.
- [10] T. Mattisson, M. Keller, C. Linderholm, P. Moldenhauer, M. Rydén, H. Leion, A. Lyngfelt, Chemical-looping technologies using circulating fluidized bed systems: Status of development, Fuel Process. Technol. 172 (2018) 1–12, <https://doi.org/10.1016/j.fuproc.2017.11.016>.
- [11] S.R. Son, S.D. Kim, Chemical-looping combustion with NiO and Fe₂O₃ in a thermobalance and circulating fluidized bed reactor with double loops, Ind. Eng. Chem. Res. 45 (8) (2006) 2689–2696, <https://doi.org/10.1021/ie050919x>.
- [12] L.S. Fan, Chemical looping systems for fossil energy conversions, John Wiley and Sons (2010), <https://doi.org/10.1002/9780470872888>.
- [13] O.A. Omoniyi, V. Dupont, Chemical looping steam reforming of acetic acid in a packed bed reactor, Appl. Catal. B 226 (2018) 258–268, <https://doi.org/10.1016/j.apcatb.2017.12.027>.
- [14] S. Noorman, M. van Sint Annaland, Kuipers, Packed Bed Reactor Technology for Chemical-Looping Combustion, Ind. Eng. Chem. Res. 46 (12) (2007) 4212–4220, <https://doi.org/10.1021/ie061178i>.
- [15] I.S. Metcalfe, B. Ray, C. Dejoie, W. Hu, C. de Leeuwe, C. Dueso, F.R. García-García, C.-M. Mak, E.I. Papaioannou, C.R. Thompson, J.S.O. Evans, Overcoming chemical equilibrium limitations using a thermodynamically reversible chemical reactor, Nat. Chem. 11 (7) (2019) 638–643, <https://doi.org/10.1038/s41557-019-0273-2>.
- [16] V. Cox, J. D., Wagman, D. D. & Medvedev, CODATA Key Values for Thermodynamics, Hemisphere Publishing Corp, New York, 1984.
- [17] M. Kuhn, S. Hashimoto, K. Sato, K. Yashiro, J. Mizusaki, Oxygen nonstoichiometry, thermo-chemical stability and lattice expansion of La_{0.6}Sr_{0.4}FeO_{3- δ} , Solid State Ionics 195 (1) (2011) 7–15, <https://doi.org/10.1016/j.ssi.2011.05.013>.

- [18] J. Mizusaki, M. Yoshihiro, S. Yamauchi, K. Fueki, Nonstoichiometry and defect structure of the perovskite-type oxides $\text{La}_{1-x}\text{Sr}_x\text{FeO}_{3-\delta}$, *J. Solid State Chem.* 58 (2) (1985) 257–266, [https://doi.org/10.1016/0022-4596\(85\)90243-9](https://doi.org/10.1016/0022-4596(85)90243-9).
- [19] M. Sogaard, P. Vang Hendriksen, M. Mogensen, Oxygen nonstoichiometry and transport properties of strontium substituted lanthanum ferrite, *J. Solid State Chem.* 180 (4) (2007) 1489–1503, <https://doi.org/10.1016/j.jssc.2007.02.012>.
- [20] C. de Leeuwe, W. Hu, D. Neagu, E.I. Papaioannou, S. Pramana, B. Ray, J.S. O. Evans, I.S. Metcalfe, Revisiting the thermal and chemical expansion and stability of $\text{La}_{0.6}\text{Sr}_{0.4}\text{FeO}_{3-\delta}$, *J. Solid State Chem.* 293 (2021) 121838, <https://doi.org/10.1016/j.jssc.2020.121838>.
- [21] P. Heidebrecht, K. Sundmacher, Thermodynamic analysis of a cyclic water gas-shift reactor (CWGSR) for hydrogen production, *Chem. Eng. Sci.* 64 (23) (2009) 5057–5065, <https://doi.org/10.1016/j.ces.2009.08.011>.
- [22] L. Zeng, F. He, F. Li, L.-S. Fan, Coal-Direct Chemical Looping Gasification for Hydrogen Production: Reactor Modeling and Process Simulation, *Energy Fuels* 26 (6) (2012) 3680–3690, <https://doi.org/10.1021/ef3003685>.
- [23] M. Saghaififar, S.A. Scott, The use of high decomposition temperature materials for Chemical Looping Electricity Storage, *Chem. Eng. J.* (2021) 128789, <https://doi.org/10.1016/j.cej.2021.128789>.
- [24] M. Pechini, Method of preparing idead and alkaline earth titanates and niobates and coating method using the same, US3330697A (1963).
- [25] J.-L. Hodeau, P. Bordet, M. Anne, A. Prat, A.N. Fitch, E. Dooryhee, G. Vaughan, A. K. Freund, Nine-crystal multianalyzer stage for high-resolution powder diffraction between 6 keV and 40 keV, *Cryst. Multilayer Opt.* 3448 (1998) 353, <https://doi.org/10.1117/12.332525>.
- [26] V. Swamy, H.J. Seifert, F. Aldinger, Thermodynamic properties of Y_2O_3 phases and the yttrium–oxygen phase diagram, *J. Alloy. Compd.* 269 (1-2) (1998) 201–207, [https://doi.org/10.1016/S0925-8388\(98\)00245-X](https://doi.org/10.1016/S0925-8388(98)00245-X).
- [27] D. Taylor, Thermal expansion data : III sesquioxides, M_2O_3 , with the corundum and the A-, B- and C- M_2O_3 structures, *Trans. J. Br. Ceram. Soc.* 83 (1984) 92.
- [28] A. Coelho, TOPAS academic: general profile and structure analysis software for powder diffraction data, 5th editio, Karlsruhe, Germany, 2012.
- [29] R.E. Dinnebier, A. Leineweber, J.S.O. Evans, Rietveld refinement: practical powder diffraction pattern analysis using TOPAS, 1st ed., De Gruyter, Berlin Boston, 2019 <https://doi.org/10.1515/9783110461381>.
- [30] O. Levenspiel, *Chemical reaction engineering*, 3rd ed., Wiley, New York, 1999.
- [31] C.L. Yaws, Yaws' Handbook of Properties of the Chemical Elements - Knovel, Knovel, 2011. <https://app.knovel.com/web/toc.v/cid:kpYHPCE007/viewerType:toc/> (accessed July 9, 2020).
- [32] E.N. Fuller, P.D. Schettler, J.C. Giddings, NEW METHOD FOR PREDICTION OF BINARY GAS-PHASE DIFFUSION COEFFICIENTS, *Ind. Eng. Chem.* 58 (5) (1966) 18–27, <https://doi.org/10.1021/ie50677a007>.
- [33] E. Marek, W. Hu, M. Gaultois, C.P. Grey, S.A. Scott, The use of strontium ferrite in chemical looping systems, *Appl. Energy* 223 (2018) 369–382, <https://doi.org/10.1016/j.apenergy.2018.04.090>.
- [34] S.V. Patankar, *Numerical heat transfer and fluid flow*, McGraw-Hill, New York, 1980.
- [35] L.F. Shampine, M.W. Reichelt, The MATLAB ODE Suite, *SIAM J. Sci. Comput.* 18 (1) (1997) 1–22, <https://doi.org/10.1137/S1064827594276424>.
- [36] D. Burgess, Thermochemical data, in: P. Linstrom, W. Mallard (Eds.), NIST Chem. WebBook, NIST Stand. Ref. Database Number 69, National Institute of Standards and Technology, Gaithersburg MD 20899, 2019, <https://doi.org/10.18434/T4D303>.